An Iterative Regularization Method based on Tensor Subspace Representation for Hyperspectral Image Super-Resolution

Ting Xu, Ting-Zhu Huang, Liang-Jian Deng, and Naoto Yokoya

Abstract—**Hyperspectral image super-resolution (HSI-SR) can be achieved by fusing a paired multispectral image (MSI) and hyperspectral image (HSI), which is a prevalent strategy. But, how to precisely reconstruct the high spatial resolution hyperspectral image (HR-HSI) by fusion technology is a challenging issue. In this paper, we propose an iterative regularization method based on tensor subspace representation (IR-TenSR) for MSI-HSI fusion, thus HSI-SR. First, we propose a tensor subspace representation (TenSR)-based regularization model that integrates the global spectral-spatial low-rank and the nonlocal self-similarity priors of HR-HSI. These two priors have been proven effective, but previous HSI-SR works cannot simultaneously exploit them. Subsequently, we design an iterative regularization procedure to utilize the residual information of acquired low-resolution images, which are ignored in other works that produce suboptimal results. Finally, we develop an effective algorithm based on the proximal alternating minimization method to solve the TenSR-regularization model. With that, we obtain the iterative regularization algorithm. Experiments implemented on the simulated and real datasets illustrate the advantages of the proposed IR-TenSR compared with state-of-the-art fusion approaches.**

Index Terms—**Hyperspectral image super-resolution, tensor subspace, nonlocal self-similarity, global spatial-spectral low-rank prior, proximal alternating minimization, iterative regularization.**

I. INTRODUCTION

Hyperspectral imaging technology has attracted much attention since it can capture hyperspectral images (HSIs) that contribute to identifying materials accurately [1]–[4]. The acquired HSIs have found a wide range of applications in remote sensing and computer vision [5]–[10]. However, there is an unavoidable tradeoff between spectral and spatial resolution for acquired HSIs, which will affect subsequent applications. Due to various hardware limitations, it is costly and challenging to improve the spatial resolution of HSIs directly. Contrary to HSIs, multispectral images (MSIs) have lower spectral resolution and higher spatial resolution. Thereby, fusing a

paired MSI and HSI has become a popular way to obtain a high spatial resolution hyperspectral image (HR-HSI). This process can be seen as hyperspectral image super-resolution (HSI-SR). The existing HSI-SR methods can be divided into deep learning (DL)-based methods, sparse representation-based methods, tensor factorization (TF)-based methods, and matrix subspace representation (MatSR)-based methods.

With the high efficiency and excellent performance of DL in computer vision tasks, such as object detection and classification, many researchers have proposed DL-based HSI-SR methods [11]–[27]. For example, Hu et al. [17] design a deep convolution neural network (CNN) that can preserve both spatial and spectral information for the HSI and MSI fusion task. The major advantage of these methods is that they can generate excellent results since CNN has a strong capacity to explore the image features. However, it is not easy to collect many training data, i.e., the paired HSI and HSI. To solve such an issue, unsupervised DL-based methods are proposed. For example, Zhang et al. [28] develop an unsupervised adaptation learning framework for the HSI-SR task. However, these methods may generate suboptimal results compared with supervised methods.

The sparse representation-based methods [29]–[34] mainly exploit the the spatial-spectral sparsity of HR-HSI. Under this framework, the HR-HSI is represented by a dictionary and the corresponding sparse coefficients. To estimate the dictionary and coefficients accurately, it is necessary to incorporate other priors. For example, Xue et al. [30] propose a structured sparse low-rank representation-based HSI-SR method that considers the spatial/spectral subspace low-rank relationships between MSI/HSI and HR-HSI. More recently, inspired by the tensor-tensor product (t-product), Xu et al. [31] propose a tensor sparse representation-based HSI-SR method that incorporates the nonlocal self-similarity and sparse prior. Dian et al. [35] propose a nonlocal sparse tensor Tucker decomposition method for the semi-blind fusion of HSI and MSI. However, these methods fail to fully capture the prior knowledge of HR-HSI, resulting in unsatisfactory HSI-SR results. In particular, it is difficult to reconstruct the details in the case of relatively low sampling ratios.

As the HR-HSI is a three-dimensional (3-D) tensor, TF-based models have attracted much attention for the HSI-SR problem. These methods mainly based on different tensor decompositions that depict the spectral and spatial correlation, Tucker decomposition [36]–[39], Canonical polyadic (CP) decomposition [40]–[42], block-term decomposition [43], tensor-

T. Xu, T.-Z. Huang, L.-J. Deng are with the Research Center for Image and Vision Computing, School of Mathematical Sciences, University of Electronic Science and Technology of China, Chengdu 611731, P.R.China (e-mail: 17742879536@163.com; tingzhuhuang@126.com; liangjian.deng@uestc.edu.cn).

N. Yokoya is with the Department of Complexity Science and Engineering, the University of Tokyo, and with Geoinformatics Unit, RIKEN Center for Advanced Intelligence Project (AIP), Japan (e-mail: yokoya@k.u-tokyo.ac.jp).

train decomposition [44], tensor-ring decomposition [45]–[47], combined with other priors to model the HSI-SR problem. These methods have generated excellent outcomes, but they are subject to specific issues. The HR-HSI has strong spectral and spatial correlations, depicted by the low-rank prior. However, previous TF-based methods captured the low-rank prior in the original image space by using tensor decomposition, leading to high computational costs because of many bands. Based on previous HSI processing works, this issue could be alleviated by projecting the original HR-HSI into a low-dimensional matrix subspace. The prior HR-HSI can be explored by regularizing the basis coefficient, largely decreasing the computational cost and enhancing spectral correlation.

The spectral vectors of target HR-HSI are highly correlated, indicating that these vectors usually live in a low-dimensional subspace. The essence of MatSR-based methods [48]–[57] are to exploit the MatSR to depict this property. The results obtained by considering only spectral correlation are limited. It is necessary to introduce other regularizers to portray other priors of HR-HSI. For example, Simo$\tilde{e}$s et al. [53] employ the total variation TV regularizer to characterize the spatial smoothness prior. Xu et al. [57] introduce the low-rank tensor ring decomposition based on tensor nuclear norm to depict the nonlocal self-similarity. MatSR-based methods project the rearranged matrix into the low-dimensional spectral subspace, generating excellent effect/efficiency tradeoffs. Compared with TF-based methods, these methods have lower computational complexity. However, MatSR-based methods meet the following drawbacks: 1) These methods only consider the correlation in the spectrum of HR-HSI and ignore the correlation in space. 2) The unfolding operation involved in MatSR-based methods would inevitably destroy the inherent HR-HSI structure.

In addition to the problems of each method analyzed above, they also have the following points that could be improved. (1) Motivated by HSI denoising methods [58]–[60], global spectral-spatial correlation, spatial structure, and nonlocal self-similarity properties have been widely considered for the task of HSI-SR. However, previous HSI-SR works cannot simultaneously capture the mentioned characteristics. For example, in [37], the authors use Tucker decomposition and ℓ_1 term to capture the first two priors while ignoring the nonlocal self-similarity prior that can depict the structured information. Dian et al. [61] employ the MatSR to capture the spectral correlation and the nonlocal low-rank regularization on the matrix coefficient to investigate the nonlocal self-similarity prior. However, it ignores the spatial correlation. (2) Previous HSI-SR works do not utilize the residual information[1] of acquired MSI and HSI. Improving the utilization of acquired image information is one of the core problems of super-resolution. However, previous HSI-SR works ignore the utilization of residual information of acquired low-resolution images, resulting in the loss of information and affecting the HSI-SR results.

---

[1] Assume the target HR-HSI $\mathcal{X}$ and its spatially and spectrally degraded versions are $\widehat{\mathcal{Y}}$ and $\widehat{\mathcal{Z}}$, respectively. The acquired HSI and MSI are $\mathcal{Y}$ and $\mathcal{Z}$, respectively. Then, we define $\mathcal{Y} - \widehat{\mathcal{Y}}$ and $\mathcal{Z} - \widehat{\mathcal{Z}}$ as the residual information of $\mathcal{Y}$ and $\mathcal{Z}$, respectively.

To address these mentioned issues, we propose an iterative regularization method based on tensor subspace representation (IR-TenSR) for HSI-SR. Specifically, we first establish a tensor subspace representation (TenSR)-based regularization model that integrates the global spectral-spatial low-rank and non-local self-similarity priors of HR-HSI. We introduce TenSR, which was effectively introduced in HSI denoising [59], such as dimension reduction and structure preservation, to depict global spectral-spatial low-rank prior. Under the framework of TenSR (see details in Section III-A), the spatial structure depiction of the original HR-HSI can be transformed to explore the representation low-dimensional tensor coefficient image. To preserve the spatial structure, we exploit the nonlocal self-similarity prior to regularizing the coefficient image. Moreover, motivated by the effectiveness of tensor nuclear norm (TNN), we apply it to describe the low-rank property of the nonlocal grouped tensor. Subsequently, we design an iterative regularization procedure based on the TenSR-based regularization model to exploit the residual information of acquired MSI and HSI. The flowchart of the proposed IR-TenSR is shown in Fig. 1 and the contributions are summarized as follows.

- We develop a TenSR-based regularization model to simultaneously depict the global spectral-spatial correlation and nonlocal self-similarity properties of HR-HSI. Thus, the reconstruction of HR-HSI is transformed to estimate the tensor subspace and tensor coefficient image. Especially, the global spectral and spatial correlation is captured by TenSR, and TNN is employed to exploit the nonlocal self-similarity property by regularizing the tensor coefficient image.
- Based on the TenSR-based regularization model, we design an iterative regularization procedure to utilize the residual information of acquired MSI and HSI, which is effective but ignored by previous HSI-SR works.
- We develop an efficient algorithm based on the proximal alternating minimization (PAM) to solve the developed TenSR-based regularization model. Equipped with that, we obtain the iterative regularization algorithm. Extensive experimental outputs on one real dataset and three simulated datasets illustrate that the proposed IR-TenSR performs better than the state-of-the-art HSI-SR approaches for quantitative and visual comparisons.

We arrange the remaining part as follows. The related work is described in Section II. We introduce the proposed IR-TenSR method in Section III. Section IV and Section V illustrate the experimental results and model discussion, respectively. Finally, we conclude this paper in Section VI.

II. RELATED WORK

A. Notations

We represent tensors, matrices, vectors, and scalars by calligraphic letter, e.g., $\mathcal{B}$, boldface capital letters, e.g., $\mathbf{B}$, boldface lowercase letters, e.g., $\mathbf{b}$, and capital or lowercase letters, e.g., B or b, respectively. The filed of real number and complex number are denoted as $\mathbb{R}$ and $\mathbb{C}$, respectively. For a three-order tensor $\mathcal{B} \in \mathbb{C}^{W \times H \times S}$, we represent (i, j, k)-th

element as $\mathcal{B}_{ijk}$ or b_{ijk}, denote the (i,j)-th tube as $\mathcal{B}(i,j,:)$, and use $\mathcal{B}(:,:,i)$, $\mathcal{B}(:,i,:)$ and $\mathcal{B}(i,:,:)$ to represent the i-th frontal slice, lateral slice and horizontal slice, respectively, for brevity, $\mathcal{B}(:,:,i)$ is written as $\mathbf{B}^{(i)}$. $\tilde{\mathcal{A}}$ represents the tensor produced by doing the discrete Fourier transformation (DFT) along the third dimension of $\mathcal{A}$, i.e., $\tilde{\mathcal{A}} = fft(\mathcal{A},[\ ],3)$. The permuted tensors of $\mathcal{M} \in \mathbb{R}^{W \times H \times S}$ are denoted as $\mathcal{M} := \text{permute}(\mathcal{M},[I,J,K])$, where $[I,J,K]$ is a random permutations of [1, 2, 3]. For example, we denote $\mathcal{M}_4$ as $\mathcal{M}_4 := \text{permute}(\mathcal{M},[1,3,2]) \in \mathbb{R}^{W \times S \times H}$. The lateral slice of $\mathcal{M}_4$ is the frontal slice of $\mathcal{M}$. Correspondingly, the inverse operation of "permute" is denoted as "ipermute", and we have $\mathcal{M} := \text{ipermute}(\mathcal{M}_4,[1,3,2])$. We denote the Frobenius norm and the tensor nuclear norm (TNN) as $||\mathcal{M}||_F = \sqrt{\sum_{ijk}|m_{ijk}|^2}$ and $||\mathcal{M}||_{\text{TNN}} = \sum_{i=1}^{S}||\tilde{\mathbf{M}}^{(i)}||_*$, respectively.

B. Definitions

The work-related definitions, lemma, and theorems are as follows.

Definition 1 (t-Product [62]): For two given tensors $\mathcal{O} \in \mathbb{R}^{W \times N \times S}$ and $\mathcal{P} \in \mathbb{R}^{N \times H \times S}$, the result of the t-product $\mathcal{O} * \mathcal{P}$ is a tensor $\mathcal{Q} \in \mathbb{R}^{W \times H \times S}$, where (i,j)-th tube of $\mathcal{Q}$ is given by

$$\mathcal{Q}(i,j,:) = \sum_{k=1}^{N} \mathcal{O}(i,k,:) * \mathcal{P}(k,j,:). \tag{1}$$

Definition 2 (Transpose Tensor [62]): For a given tensor $\mathcal{O} \in \mathbb{R}^{W \times H \times S}$, transpose tensor $\mathcal{O}^T \in \mathbb{R}^{H \times W \times S}$ is obtained by transposing each frontal slice of $\mathcal{O}$ and then reversing the order of transposed frontal slices 2 through S.

Definition 3 (Identity Tensor [62]): For a given tensor $\mathcal{I} \in \mathbb{R}^{M \times M \times S}$, if it's first frontal slice is identity matrix and other frontal slices are zeros, this tensor $\mathcal{I}$ is called as identity tensor.

Definition 4 (Orthogonal Tensor [62]): Gicen a tensor $\mathcal{M} \in \mathbb{R}^{M \times M \times S}$, it is an orthogonal tensor if $\mathcal{M} * \mathcal{M}^T = \mathcal{M}^T * \mathcal{M} = \mathcal{I}$.

Definition 5 (F-diagonal Tensor [62]): For a given tensor $\mathcal{Q} \in \mathbb{R}^{W \times H \times S}$, if each of its frontal slices is a diagonal matrix, this tensor $\mathcal{Q}$ is called f-diagonal.

Lemma 1: [62] For two given tensors $\mathcal{G} \in \mathbb{R}^{W \times N \times S}$ and $\mathcal{H} \in \mathbb{R}^{N \times H \times S}$, if $\mathcal{G}$ is orthogonal, we have

$$||\mathcal{G} * \mathcal{H}||_F = ||\mathcal{H}||_F. \tag{2}$$

Theorem 1 (t-SVD [62]): For a given tensor $\mathcal{M} \in \mathbb{R}^{W \times H \times S}$, the t-SVD of $\mathcal{M}$ is

$$\mathcal{M} = \mathcal{U} * \mathcal{S} * \mathcal{V}^T. \tag{3}$$

where $\mathcal{U} \in \mathbb{R}^{W \times W \times S}$ and $\mathcal{V} \in \mathbb{R}^{H \times H \times S}$ are orthogonal, $\mathcal{S} \in \mathbb{R}^{W \times H \times S}$ is f-diagonal.

Definition 6 (Tensor Tubal Rank [63]): For a given tensor $\mathcal{M} \in \mathbb{R}^{W \times H \times S}$, its tensor tubal rank is defined as the number of nonzero singular tubes of $\mathcal{S}$, that is

$$rank_t(\mathcal{M}) = \#\{j, \mathcal{S}(j,j,:) \neq 0\}, \tag{4}$$

where $\mathcal{S}$ comes from the t-SVD of $\mathcal{M}$, i.e., $\mathcal{M} = \mathcal{U} * \mathcal{S} * \mathcal{V}^T$.

Theorem 2 [59]: For any $\mathcal{B} \in \mathbb{R}^{m_1 \times m_2 \times m_3}$, the following problem:

$$\underset{\mathcal{B}}{\arg\min} \frac{1}{2}||\mathcal{A} - \mathcal{B} * \mathcal{C}||_F^2 + \frac{\beta}{2}||\mathcal{B} - \mathcal{C}||_F^2, \tag{5}$$
$$s.t. \quad \mathcal{B}^T \mathcal{B} = \mathcal{I},$$

has a closed-form solution $\mathcal{B}^* = \mathcal{V} * \mathcal{U}^T$, where $\mathcal{U}$ and $\mathcal{V}$ come from the t-SVD of $\mathcal{C} * \mathcal{A}^T + \beta \mathcal{C}^T = \mathcal{U} * \mathcal{S} * \mathcal{V}^T$.

Theorem 3 (TNN-based t-SVT [64]): For a three-order tensor $\mathcal{B} \in \mathbb{R}^{m_1 \times m_2 \times m_3}$, a minimizer to

$$\underset{\mathcal{B}}{\arg\min} \alpha||\mathcal{B}||_{\text{TNN}} + \frac{1}{2}||\mathcal{B} - \mathcal{C}||_F^2, \tag{6}$$

which has a closed-form solution

$$\mathcal{B} = \mathcal{U} * \mathcal{S}_{\text{TNN}}^\alpha * \mathcal{V}^T, \tag{7}$$

where $\mathcal{C} = \mathcal{U} * \mathcal{S} * \mathcal{V}^T$, $\tilde{\mathcal{S}}_{\text{TNN}}^\alpha = \max(\tilde{\mathcal{S}} - \alpha, 0)$, $\tilde{\mathcal{S}} = \text{fft}(\mathcal{S},[\ ],3)$, and $\mathcal{S}_{\text{TNN}}^\alpha = \text{ifft}(\tilde{\mathcal{S}}_{\text{TNN}}^\alpha,[\ ],3)$.

C. Problem Formulation

In this paper, we focus on the HSI-SR task by fusing a pair of HSI ($\mathcal{Y} \in \mathbb{R}^{w \times h \times S}$) and MSI ($\mathcal{Z} \in \mathbb{R}^{W \times H \times s}$) to generate the HR-HSI ($\mathcal{X} \in \mathbb{R}^{W \times H \times S}$).

1) Observation Model: $\mathcal{Y} \in \mathbb{R}^{w \times h \times S}$ represents the HSI with $w \times h$ pixels and S bands. In particular, $\mathcal{Y}$ can be regarded as the spatially degraded version of HR-HSI $\mathcal{X} \in \mathbb{R}^{W \times H \times S}$ with $W \times H$ pixels and S bands, i.e.,

$$\mathbf{Y}_{(3)} = \mathbf{X}_{(3)}\mathbf{BS} + \mathbf{N}_1, \tag{8}$$

where $\mathbf{X}_{(3)} \in \mathbb{R}^{S \times WH}$ and $\mathbf{Y}_{(3)} \in \mathbb{R}^{S \times wh}$ are matrices obtained by unfolding HR-HSI $\mathcal{X}$ and HSI $\mathcal{Y}$ along the spectral (third) dimension, respectively. $\mathbf{S} \in \mathbb{R}^{WH \times wh}$ is a spatial degraded matrix. $\mathbf{B} \in \mathbb{R}^{WH \times WH}$ is a spatial blurring kernel, which is band-independent and under circular boundary conditions. $\mathbf{N}_1$ denotes independent and identically distributed (i.i.d.) noise. For simplicity, we reformulate (8) as

$$\mathcal{Y} = \mathcal{H}(\mathcal{X}) + \mathcal{N}_1, \tag{9}$$

where $\mathcal{H}(\cdot)$ is spatially degraded operator, $\mathcal{N}_1$ is the noises contained in the observed HSI.

$\mathcal{Z} \in \mathbb{R}^{W \times H \times s}$ denotes the MSI with $W \times H$ pixels and s bands. $\mathcal{Z}$ can be treated as the spectrally degraded version of HR-HSI $\mathcal{X}$, i.e.,

$$\mathbf{Z}_{(3)} = \mathbf{R}\mathbf{X}_{(3)} + \mathbf{N}_2, \tag{10}$$

where $\mathbf{R} \in \mathbb{R}^{s \times S}$ is spectral response matrix and $\mathbf{N}_2$ denotes i.i.d. noise. For simplicity, we reformulate (10) as

$$\mathcal{Z} = \mathcal{R}(\mathcal{X}) + \mathcal{N}_2, \tag{11}$$

where $\mathcal{R}(\cdot)$ denotes the spectrally degraded operator. $\mathcal{N}_2$ is the noises contained in MSI.
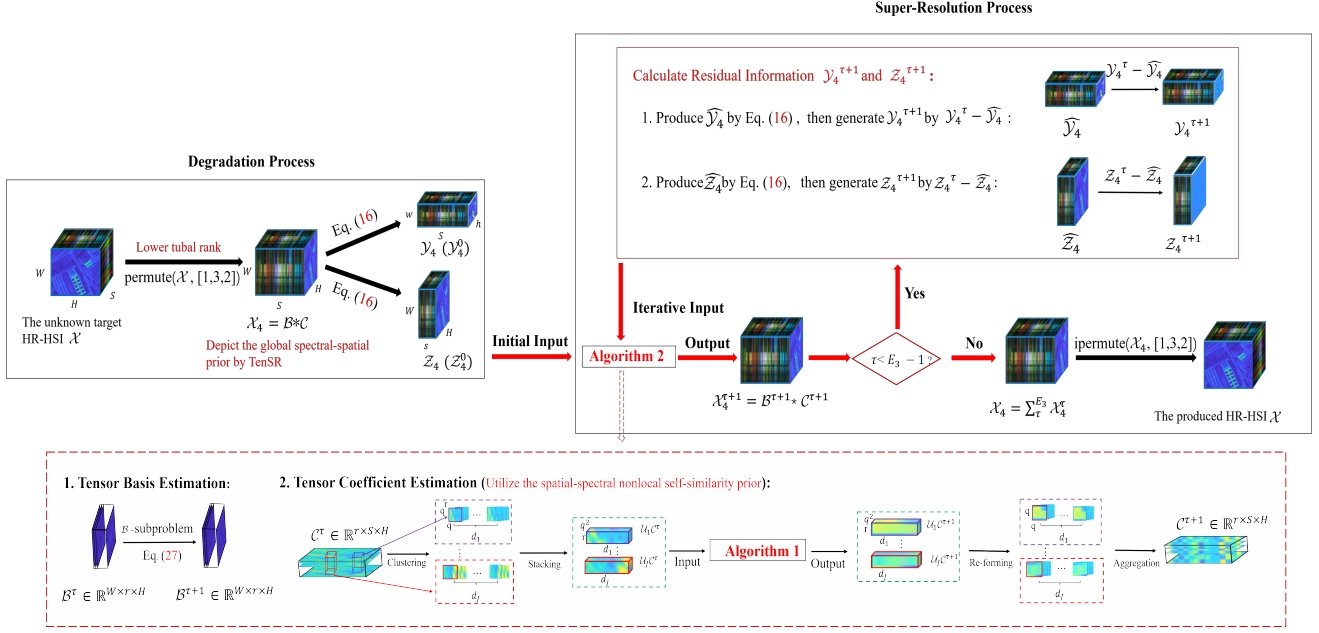
Fig. 1. Flowchart of the proposed IR-TenSR.

2) The General HSI-SR Model: Directly estimating HR-HSI from acquired HSI and MSI is an ill-posed issue, and some regularizes should be introduced to make the problem as well posed. Thus, we can formulate the general HSI-SR model as

$$\underset{\mathcal{X}}{\operatorname{argmin}} \; \frac{1}{2}||\mathcal{Y} - \mathcal{H}(\mathcal{X})||_F^2 + \frac{1}{2}||\mathcal{Z} - \mathcal{R}(\mathcal{X})||_F^2 + \mu \mathcal{J}(\mathcal{X}),$$
(12)

where the first two terms are called fidelity term, regularization term $\mathcal{J}(\mathcal{X})$ is used to depict the latent priors of the target HR-HSI $\mathcal{X}$, and μ is a regularization parameter.

III. PROPOSED ITERATIVE REGULARIZATION METHOD BASED ON TENSOR SUBSPACE REPRESENTATION FOR HSI-SR

A. TenSR Model for HSI-SR

1) TenSR: TenSR represents the tensor $\mathcal{X} \in \mathbb{R}^{W \times H \times S}$ by t-product over a tensor basis and the corresponding tnesor coefficient [59], i.e.,

$$\mathcal{X} = \overline{\mathcal{B}} * \overline{\mathcal{C}},$$
(13)

where $\overline{\mathcal{B}} \in \mathbb{R}^{W \times r \times S}$ and $\overline{\mathcal{C}} \in \mathbb{R}^{r \times H \times S}$ denote the tensor basis and tensor coefficient, respectively, in which $\mathcal{B}$ is orthogonal. r is the subspace dimension, which is described by the tubal rank of $\mathcal{X}$.

2) Low Tubal Rankness: Since the subspace dimension of TenSR is related to the tubal rank, which is different if the spectral mode lies in different dimensions (e.g., the spectral mode is in the first mode rather than in the third mode) [59]. In this part, we discuss the low tubal rankness with the spectral mode in different dimensions. Given an HSI tensor $\mathcal{X} \in \mathbb{R}^{W \times H \times S}$, we define the following five permuted tensors:

$$\begin{aligned}
\mathcal{X}_1 &:= \operatorname{permute}(\mathcal{X}, [2, 1, 3]) \in \mathbb{R}^{H \times W \times S}, \\
\mathcal{X}_2 &:= \operatorname{permute}(\mathcal{X}, [3, 1, 2]) \in \mathbb{R}^{S \times W \times H}, \\
\mathcal{X}_3 &:= \operatorname{permute}(\mathcal{X}, [3, 2, 1]) \in \mathbb{R}^{S \times H \times W}, \\
\mathcal{X}_4 &:= \operatorname{permute}(\mathcal{X}, [1, 3, 2]) \in \mathbb{R}^{W \times S \times H}, \\
\mathcal{X}_5 &:= \operatorname{permute}(\mathcal{X}, [2, 3, 1]) \in \mathbb{R}^{H \times S \times W}.
\end{aligned}$$
(14)

We select seven HR-HSIs and present the tensor singular values of $\mathcal{X}$, $\mathcal{X}_1$, $\mathcal{X}_2$, $\mathcal{X}_3$, $\mathcal{X}_4$, and $\mathcal{X}_5$ in Fig. 2. Note that tensor singular values of $\mathcal{X}$ are the entries on the diagonal of the average of all front slice of $\mathcal{S}$ (i.e., $\frac{1}{S}\sum_{i=1}^{S} \mathcal{S}^{(i)}$), where $\mathcal{S}^{(i)}$ comes from the t-SVD of $\mathcal{X} = \mathcal{U} * \mathcal{S} * \mathcal{V}^T$. By Fig. 2 (c)-(f), we find that $\mathcal{X}_2$, $\mathcal{X}_3$, $\mathcal{X}_4$, and $\mathcal{X}_5$, have lower tubal rank than $\mathcal{X}$ and $\mathcal{X}_1$. The result implies that the tensor whose spectral dimension is in mode-1 or mode-2 has a lower tubal rank. Through experimental analysis (see details in Section V-A), we find that permuted tensor $\mathcal{X}_4$ has better performance than others.

Thus, in this work, we assume that the permuted target HR-HSI $\mathcal{X}_4 \in \mathbb{R}^{W \times S \times H}$ (i.e., $\mathcal{X}_4$) can be represented by

$$\mathcal{X}_4 = \mathcal{B} * \mathcal{C},$$
(15)

where $\mathcal{B} \in \mathbb{R}^{W \times r \times H}$ denotes the tensor basis with r basis vectors ($r << S$), and $\mathcal{C} \in \mathbb{R}^{r \times S \times H}$ is the tensor coefficient. Thus, the permuted observed HSI $\mathcal{Y}_4 \in \mathbb{R}^{w \times S \times h}$ and MSI $\mathcal{Z}_4 \in \mathbb{R}^{W \times s \times H}$ can be represented by

$$\begin{aligned}
\mathcal{Y}_4 &= \mathcal{H}(\mathcal{X}_4) + \mathcal{N}_{14} = \mathcal{H}(\mathcal{B} * \mathcal{C}) + \mathcal{N}_{14}, \\
\mathcal{Z}_4 &= \mathcal{R}(\mathcal{X}_4) + \mathcal{N}_{24} = \mathcal{R}(\mathcal{B} * \mathcal{C}) + \mathcal{N}_{24},
\end{aligned}$$
(16)

where $\mathcal{N}_{14} := \operatorname{permute}(\mathcal{N}_1, [1, 3, 2])$ and $\mathcal{N}_{24} := \operatorname{permute}(\mathcal{N}_2, [1, 3, 2])$.
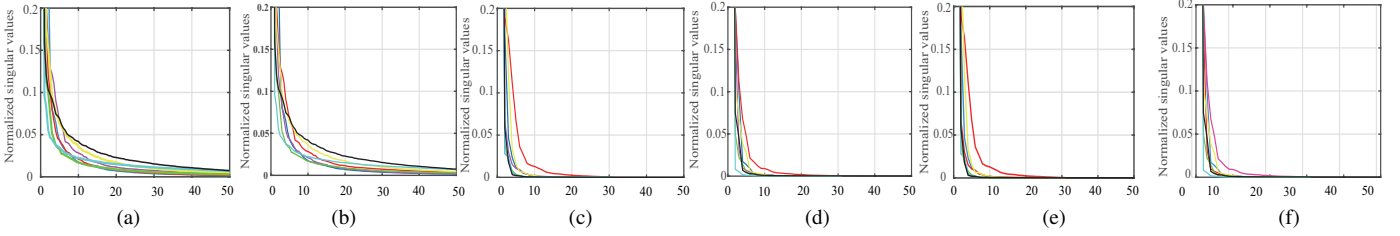
Fig. 2. Statistical analysis of low tensor tubal rank on seven HR-HSIs (the same color represents the same dataset). (a)-(f) Normalized tensor singular value curve of original HR-HSI $\mathcal{X}$ and permuted HR-HSIs $\mathcal{X}_1$, $\mathcal{X}_2$, $\mathcal{X}_3$, $\mathcal{X}_4$, and $\mathcal{X}_5$, respectively.

3) TenSR Model for HSI-SR: Based on the formulation (16), the HSI-SR problem is transferred to estimate the tensor subspace $\mathcal{B}$ and the tensor coefficient $\mathcal{C}$ from the observed MSI and HSI. Specifically, the TenSR-based HSI-SR model can be modeled as

$$\min_{\mathcal{B},\mathcal{C}} \frac{1}{2}||\mathcal{Y}_4 - \mathcal{H}(\mathcal{B} * \mathcal{C})||_F^2 + \frac{1}{2}||\mathcal{Z}_4 - \mathcal{R}(\mathcal{B} * \mathcal{C})||_F^2,$$
$$s.t. \quad \mathcal{B}^T * \mathcal{B} = \mathcal{I}. \tag{17}$$

B. Motivations

1) TenSR model for HSI-SR: In this part, we look into (17) and see the insights into why the proposed TenSR model can beat MatSR in HSI-SR. To illustrate the superiority of TenSR compared with MatSR, we test TenSR model and MatSR model that generated by replace the TenSR in model (17) by MatSR [53] on Harvard dataset [65]. Fig. 3 (a) shows the diagram of TenSR and MatSR; Fig. 3 (b) presents the HSI-SR results by these two subspaces under different subspace dimensions. From this figure, we find that the performance of TenSR is better than MatSR, and the reason is that TenSR is a more authentic representation for delivering the intrinsic structure of HR-HSI since MatSR only considers the correlation in the spectrum of HR-HSI, ignoring the correlation in space. Motivated by the above observation, we would like to apply TenSR to HSI-SR.

2) Nonlocal Low-Rank Regularization for HSI-SR: TenSR only consider the correlation of spectrum and space, which is insufficient. Thus, we need to dig out other priors of HR-HSI. The nonlocal self-similarity has been proven to be effective in HSI-SR problem [36], [61]. Under the framework of TenSR, the tensor coefficient image $\mathcal{C}$ inherits the latent property of the permuted HR-HSI $\mathcal{X}_4$. Thus, we will verify the nonlocal self-similarity prior of HR-HSI on tensor coefficient image $\mathcal{C} \in \mathbb{R}^{r \times S \times H}$. Specifically, 1) Segment the tensor coefficient $\mathcal{C}$ as K overlapped cubes $\mathcal{C}_i \in \mathbb{R}^{p \times p \times r}$, $i = 1, 2, \cdots, K$; 2) Cluster K cubes into Λ classes with d_j ($\sum_{j=1}^{\Lambda} d_j = K$) similar cubes in each class; and 3) Stacke similar cubes in each class to form tensor $\mathcal{U}_j \mathcal{C} \in \mathbb{R}^{d_i \times r \times p^2}$; 4) Perform t-SVD on $\mathcal{U}_j \mathcal{C}$, $j = 1, 2, \cdots, \Lambda$. The whole process can be seen in Fig. 4, and we find that tensors $\mathcal{U}_j \mathcal{C}$ ($j = 1, \cdots, \Lambda$) are low-rank. Therefore, we introduce the TNN on grouped tensor $\mathcal{U}_j \mathcal{C}$ to depict the nonlocal self-similarity prior. This strategy can reduce the computational complexity compared with directly employing the nonlocal regularizer to HR-HSI [66].
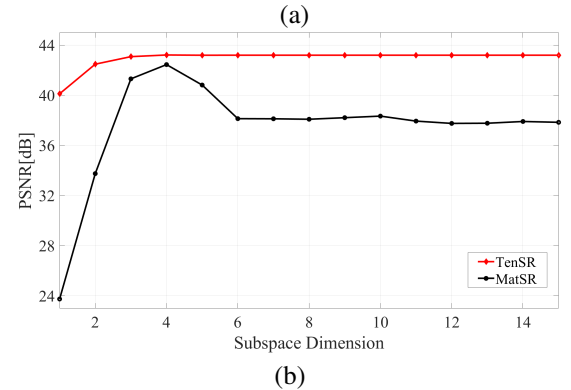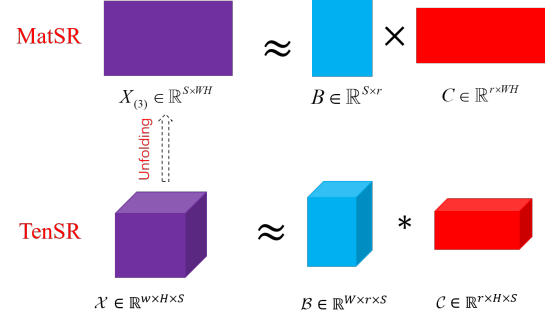

(a)

(b)

Fig. 3. (a) shows the diagram of TenSR and MatSR; (b) reports the HSI-SR results by using TenSR and MatSR with different subspace dimensions.

3) Residual Information for HSI-SR: HSI-MSI fusion technology aims to utilize the available HSI and MSI to enhance the spatial resolution of HSI. Therefore, how to improve the utilization of low-resolution image information is one of the core problems [67]–[69]. Residual information, defined as the difference between the downsampled HR-HSI and the acquired low-resolution images, usually exists between the downsampled HR-HSI and the acquired HSI and MSI. However, the existing HSI-SR methods only focus on designing the regularization terms, ignoring the value of residual information. To solve such an issue, we develop an iterative regularization procedure to utilize the residual information, and the details are shown in Section III-C.

C. Iterative Regularization Procedure

1) TenSR-based Regularization Model: By concatenating the global spectral-spatial correlation and nonlocal self-
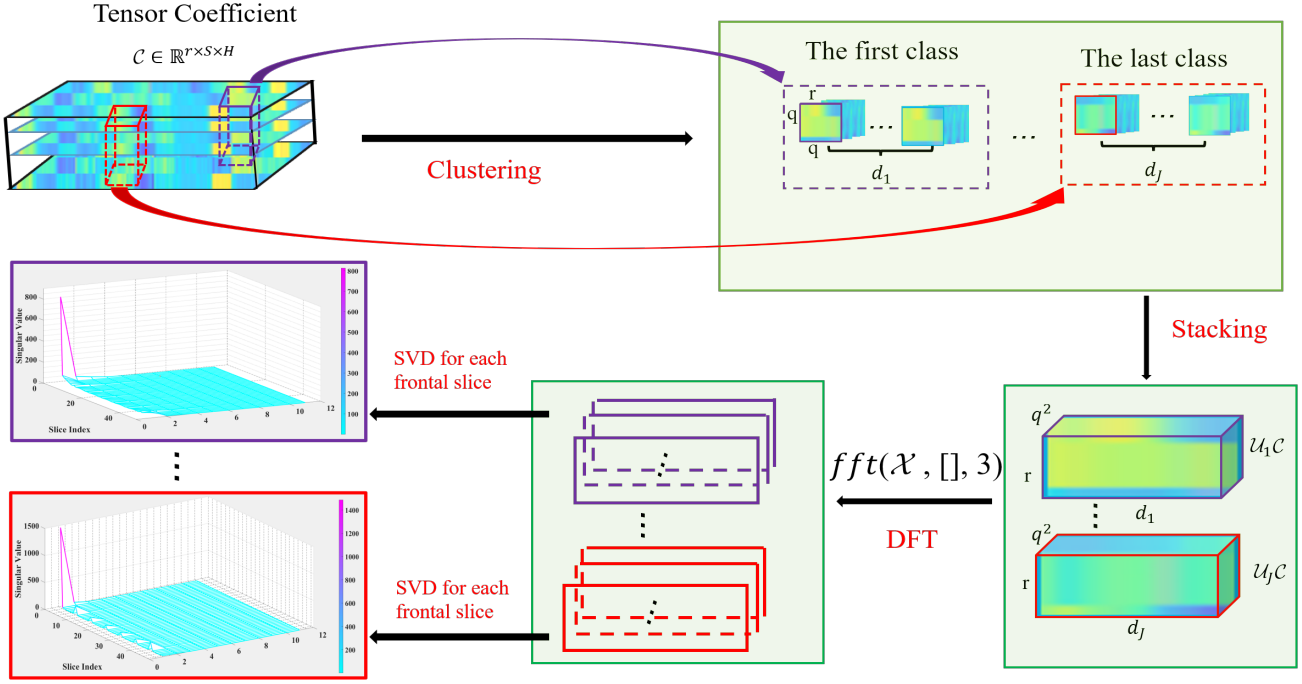
Fig. 4. Spatial-spectral nonlocal self-similarity property of the tensor coefficient.

similarity property of HR-HSI, the proposed TenSR-based regularization model is formulated as

$$\min_{\mathcal{B},\mathcal{C}} \frac{1}{2}||\mathcal{Y}_4 - \mathcal{H}(\mathcal{B}*\mathcal{C})||_F^2 + \frac{1}{2}||\mathcal{Z}_4 - \mathcal{R}(\mathcal{B}*\mathcal{C})||_F^2 + \lambda\mathcal{J}(\mathcal{C}),$$
$$s.t. \quad \mathcal{B}^T * \mathcal{B} = \mathcal{I}, \tag{18}$$

where λ denotes a positive regularization parameter, and $\mathcal{J}(\mathcal{C}) = \sum_j^\Lambda ||\mathcal{U}_j\mathcal{C}||_{\text{TNN}}$. The permuted HR-HSI is generated by $\mathcal{X}_4 = \mathcal{B}*\mathcal{C}$.

2) Iterative Regularization Produce: Based on the model (18), we designed an iterative regularization procedure. Firstly, calculate $\mathcal{X}_4^1$ as a minimizer of the TenSR-based regularization model (18) by a paired permuted HSI $\mathcal{Y}_4$ and MSI $\mathcal{Z}_4$. Secondly, degenerate $\mathcal{X}_4^1$ by (16) to generate $\widehat{\mathcal{Y}_4}$ and $\widehat{\mathcal{Z}_4}$. Thirdly, compute the residual information $(\mathcal{Y}_4 - \widehat{\mathcal{Y}_4})$ and $(\mathcal{Z}_4 - \widehat{\mathcal{Z}_4})$ as the data input to the model (18) to obtain $\mathcal{X}_4^2$. This process is repeated until the maximum number of iterations (E_3) is reached. Finally, we generate the target HR-HSI $\mathcal{X}$ by ipermute$(\sum_{\tau=1}^{E_3} \mathcal{X}_4^\tau, [1,3,2])$. We summarize the whole procedure as follows:

- Initialize: $\mathcal{Y}_4^0 = \mathcal{Y}_4$, $\mathcal{Z}_4^0 = \mathcal{Z}_4$.
- For $\tau = 0, 1, 2, \cdots, E_3$
  1. Compute $\mathcal{X}_4^{\tau+1}$ as a minimizer of the TenSR-based regularization model (18).
  2. Downgrade $\mathcal{X}_4^{\tau+1}$ to obtain $\widehat{\mathcal{Y}_4}$ and $\widehat{\mathcal{Z}_4}$ by Eq. (16).
  3. Calculate the residual information, i.e., update $\mathcal{Y}_4^{\tau+1}$ and $\mathcal{Z}_4^{\tau+1}$ by $\mathcal{Y}_4^\tau$-$\widehat{\mathcal{Y}_4}$ and $\mathcal{Z}_4^\tau$-$\widehat{\mathcal{Z}_4}$, respectively.
- end
- Produce $\mathcal{X}$ by ipermute$(\sum_{\tau=1}^{E_3} \mathcal{X}_4^\tau, [1,3,2])$.

Subsequently, we design the optimization algorithm for the developed TenSR-based regularization model (18), then embed the designed algorithm into the iterative regularization procedure to generate the regularization algorithm.

D. Optimization Algorithm for Model (18)

Since the half-quadratic splitting technique has successfully applied in image processing problem [70], we adopt it to relax the formula (18) by introducing an auxiliary variable $\mathcal{A} = \mathcal{B}*\mathcal{C}$, i.e.,

$$\{\mathcal{A}^*, \mathcal{B}^*, \mathcal{C}^*\} = \underset{\mathcal{A},\mathcal{B},\mathcal{C}}{\operatorname{argmin}} \quad G(\mathcal{A},\mathcal{B},\mathcal{C}), \tag{19}$$

where G is

$$G(\mathcal{A},\mathcal{B},\mathcal{C}) = \frac{1}{2}||\mathcal{Y}_4 - \mathcal{H}(\mathcal{A})||_F^2 + \frac{1}{2}||\mathcal{Z}_4 - \mathcal{R}(\mathcal{A})||_F^2 + \lambda\mathcal{J}(\mathcal{C})$$
$$+ \frac{\mu}{2}||\mathcal{A} - \mathcal{B}*\mathcal{C}||_F^2,$$
$$s.t. \quad \mathcal{B}^T * \mathcal{B} = \mathcal{I}, \tag{20}$$

the last quadratic term (i.e., $\frac{\mu}{2}||\mathcal{A} - \mathcal{B}*\mathcal{C}||_F^2$) encourages $\mathcal{A}$ to approach $\mathcal{B}*\mathcal{C}$, and μ denotes a positive hyper-parameter.

We propose an algorithm based on PAM for problem (20). Each of the subproblems can be updated as follows.

1) $\mathcal{A}$-Subproblem:

$$\mathcal{A}^{k+1} = \underset{\mathcal{A}}{\operatorname{argmin}} \frac{1}{2}||\mathcal{Y}_4 - \mathcal{H}(\mathcal{A})||_F^2 + \frac{1}{2}||\mathcal{Z}_4 - \mathcal{R}(\mathcal{A})||_F^2$$
$$+ \frac{\mu}{2}||\mathcal{A} - \mathcal{B}^k * \mathcal{C}^k||_F^2 + \frac{\beta}{2}||\mathcal{A} - \mathcal{A}^k||_F^2, \tag{21}$$

where β is a proximal parameter. Problem (21) is a quadratic regularized least-square problem and can be transferred to

$$\mathcal{H}^*\mathcal{H}(\mathcal{A}) + \mathcal{R}^*\mathcal{R}(\mathcal{A}) + (\mu + \beta)\mathcal{A} =$$
$$\mathcal{H}^*(\mathcal{Y}_4) + \mathcal{R}^*(\mathcal{Z}_4) + \mu(\mathcal{B}^k * \mathcal{C}^k) + \beta\mathcal{A}^k, \tag{22}$$

where $\mathcal{H}^*$ is the adjoint of $\mathcal{H}$. Formula (22) is a Sylvester equation with an analytical and efficient solution [44].

2) $\mathcal{B}$-Subproblem:

$$\mathcal{B}^{k+1} = \underset{\mathcal{B}}{\arg\min} \ \frac{\mu}{2}||\mathcal{A} - \mathcal{B} * \mathcal{C}^{k+1}||_F^2 + \frac{\beta}{2}||\mathcal{B} - \mathcal{B}^k||_F^2,$$
$$s.t. \ \ \mathcal{B}^T * \mathcal{B} = \mathcal{I}. \tag{23}$$

By **Theorem 2**, problem (23) has closed-form solution

$$\mathcal{B}^{k+1} = \mathcal{V} * \mathcal{U}^T, \tag{24}$$

where $\mathcal{U}$ and $\mathcal{V}$ come from the t-SVD of $\mathcal{C}^{k+1} * \mathcal{A}^T + \frac{\beta}{\mu}(\mathcal{B}^k)^T = \mathcal{U} * \mathcal{S} * \mathcal{V}^T$.

3) $\mathcal{C}$-Subproblem:

$$\mathcal{C}^{k+1} = \underset{\mathcal{C}}{\arg\min} \ \lambda \mathcal{J}(\mathcal{C}) + \frac{\mu}{2}||\mathcal{A}^{k+1} - \mathcal{B}^k * \mathcal{C}||_F^2 + \frac{\beta}{2}||\mathcal{C} - \mathcal{C}^k||_F^2$$

$$= \underset{\mathcal{C}}{\arg\min} \ \lambda \sum_i^{\Lambda} ||\mathcal{U}_i \mathcal{C}||_{\text{TNN}} + \frac{\mu}{2}||\mathcal{A}^{k+1} - \mathcal{B}^k * \mathcal{C}||_F^2$$

$$+ \frac{\beta}{2}||\mathcal{C} - \mathcal{C}^k||_F^2. \tag{25}$$

Since $\mathcal{B}$ is orthogonal, by using **Lemma 1**, problem (25) is equivalent to

$$\mathcal{C}^{k+1} = \underset{\mathcal{C}}{\arg\min} \ \lambda \sum_i^{\Lambda} ||\mathcal{U}_i \mathcal{C}||_{\text{TNN}} + \frac{\mu}{2}||(\mathcal{B}^k)^T * \mathcal{A}^{k+1} - \mathcal{C}||_F^2$$

$$+ \frac{\beta}{2}||\mathcal{C} - \mathcal{C}^k||_F^2. \tag{26}$$

For simplicity, we denote $\tilde{\mathcal{C}} = [\mu(\mathcal{B}^k)^T * \mathcal{A}^{k+1} + \beta \mathcal{C}^k]/(\mu + \beta)$. The alternating direction method of multipliers (ADMM) is adopted to problem (26) with global convergence guarantee. By introducing auxiliary variables $\mathcal{N}_i = \mathcal{U}_i \mathcal{C} (i = 1, 2, \cdots, \Lambda)$, we have

$$\underset{\mathcal{N}_i, \ \mathcal{C}}{\arg\min} \ \frac{\lambda}{\mu + \beta} \sum_i^{\Lambda} ||\mathcal{N}_i||_{\text{TNN}} + \frac{1}{2}||\tilde{\mathcal{C}} - \mathcal{C}||_F^2,$$
$$s.t. \ \mathcal{N}_i = \mathcal{U}_i \mathcal{C}. \tag{27}$$

Then we have

$$L(\mathcal{N}_i, \ \mathcal{C}, \mathcal{O}_i) = \frac{\lambda}{\mu + \beta} \sum_i^{\Lambda} ||\mathcal{N}_i||_{\text{TNN}} + \frac{1}{2}||\tilde{\mathcal{C}} - \mathcal{C}||_F^2$$

$$+ \frac{\gamma}{2} \sum_i^{\Lambda} ||\mathcal{N}_i - \mathcal{U}_i \mathcal{C} + \frac{(\mathcal{O}_i)^t}{\gamma})||_F^2, \tag{28}$$

where $\gamma > 0$ is the penalty parameter and $\mathcal{O}_i$ denotes the Lagrangian multiplier. Under the ADMM framework, $\mathcal{N}_i$, $\mathcal{C}$, $\mathcal{O}_i$ are alternately updated as

$$\begin{cases} \mathcal{N}_i^{t+1} = \underset{\mathcal{N}_i}{\arg\min} \ L(\mathcal{N}_i, \ \mathcal{C}^t, \mathcal{O}_i^t), \\ \mathcal{C}^{t+1} = \underset{\mathcal{C}}{\arg\min} \ L(\mathcal{N}_i^{t+1}, \ \mathcal{C}, \mathcal{O}_i^t), \\ \mathcal{O}_i^{t+1} = \mathcal{O}_i^t + \gamma(\mathcal{N}_i^{t+1} - \mathcal{U}_i \mathcal{C}^{t+1}). \end{cases} \tag{29}$$

Algorithm 1 ADMM Algorithm to Solve Problem (25).

Input: γ.
Initialize: $\mathcal{C}^0 = \tilde{\mathcal{C}}$, $\mathcal{O}^0 = 0$.
1: **for** $t = 1 \rightarrow T$ **do**
2:     Update $\mathcal{N}_i^{t+1}$ by (30), $i = 1, 2, \cdots, \Lambda$.
3:     Update $\mathcal{C}^{t+1}$ by (32).
4:     Update $\mathcal{O}_i^{t+1}$ by (29).
5: **end for**
Output: $\mathcal{C}^{k+1}$.

Algorithm 2 PAM Algorithm to solve problem (19).

Input: Permuted HSI $\mathcal{Y}_4$, Permuted MSI $\mathcal{Z}_4$, regularization parameter λ, proximal parameter μ and β.
Initialize: $\mathcal{B}^0$, $\mathcal{C}^0 = (\mathcal{B}^0)^T * \mathcal{X}_4^{pre}$, $\mathcal{A}^0 = \mathcal{B}^0 * \mathcal{C}^0$.
1: **while** $Relcha > 10^{-3}$ and $k < E_2$ **do**
2:     Update $\mathcal{A}^{k+1}$ by (22).
3:     Update $\mathcal{B}^{k+1}$ by (23).
4:     Update $\mathcal{C}^{k+1}$ by (25).
5: **end while**
Output: $\mathcal{X}_4^{k+1} = \mathcal{B}^{k+1} * \mathcal{C}^{k+1}$.

For $\mathcal{N}_i$-subproblem, we have

$$\mathcal{N}_i^{t+1} = \underset{\mathcal{N}_i}{\arg\min} \ \frac{\gamma(\mu + \beta)}{2\lambda}||\mathcal{N}_i - \mathcal{U}_i \mathcal{C}^t + \frac{(\mathcal{O}_i)^t}{\gamma})||_F^2$$
$$+ \sum_i ||\mathcal{N}_i||_{\text{TNN}}. \tag{30}$$

Based on **Theorem 3**, let the t-SVD of $(\mathcal{U}_i \mathcal{C}^t - \frac{(\mathcal{O}_i)^t}{\gamma})$ be $\mathcal{U} * \mathcal{S} * \mathcal{V}^T$, the solution of problem (30) is given by

$$\mathcal{N}_i^{t+1} = \mathcal{U} * \mathcal{P} * \mathcal{V}^T, \tag{31}$$

where $\mathcal{P}$ is an f-diagonal tensor whose elements on the diagonal of each frontal slice in the Fourier domain is $\tilde{\mathcal{P}}(i, i, k) = \max(\tilde{\mathcal{S}}(i, i, k) - \frac{\lambda}{\gamma(\mu + \beta)}, 0)$.

$\mathcal{C}$-subproblem can be updated by

$$\mathcal{C}^{t+1} = \underset{\mathcal{C}}{\arg\min} \ \frac{1}{2}||\tilde{\mathcal{C}} - \mathcal{C}||_F^2$$

$$+ \frac{\gamma}{2} \sum_i ||\mathcal{U}_i \mathcal{C} - ((\mathcal{N}_i)^{t+1} + \frac{(\mathcal{O}_i)^t}{\gamma})||_F^2. \tag{32}$$

Problem (32) is related to a quadratic minimization problem, which can be solved directly. The algorithm for $\mathcal{C}$-subproblem (25) is summarized in Algorithm 1.

E. Initialization and Iterative Regularization Algorithm

The proposed model (18) is nonconvex. Thus, we need to use "initialize+iterative regularization" to reduce the time-consuming and improve accuracy.

1) Initialization: We initialize the tensor basis $\mathcal{B}^0$ from $\mathcal{X}^{pre}$ and learn $\mathcal{B}^0 = \mathcal{U}^0(:, 1 : r, :)$, where r is the subspace dimension and $\mathcal{U}^0$ comes from the t-SVD of $\mathcal{X}_4^{pre} = \mathcal{U}^0 * \mathcal{S}^0 * (\mathcal{V}^0)^T$. The preprocessed data $\mathcal{X}^{pre}$ is generated by the d-times cubic interpolation of the observed HSI, where d denotes the ratio of spatial dimension of MSI and HSI (i.e., W/w or H/h). We initialize the tensor coefficient $\mathcal{C}^0$ by the

projecting the preprocessed data $\mathcal{X}^{pre}$ on the subspace. The PAM algorithm-based to solve the formula (19) is presented in Algorithm 2.

Termination conditions of Algorithm 2. We define the relative change ($Relcha$) as

$$Relcha = \frac{||\mathcal{X}_4^{k+1} - \mathcal{X}_4^k||^2}{||\mathcal{X}_4^k||^2}, \qquad (33)$$

where k denotes the number of iterations.

Algorithm 2 will break out if it reaches the maximum number of iterations K (we set it to 100), or $Relcha$ is less than the tolerance (we set it to 10^{-3}).

2) Iterative Regularization Algorithm: We produce the iterative algorithm by embedding Algorithm 2 into the iterative regularization procedure, as shown in Algorithm 3. When E_3 is set as 1, Algorithm 3 downgrades to Algorithm 2. Based on the iterative regularization procedure and Algorithm 3, we obtain the proposed IR-TenSR.

F. Complexity Analysis

For Algorithm 2, the most time-consuming step is updating $\mathcal{A}$ by (22), $\mathcal{B}$ by (23), and $\mathcal{C}$ by (25). To calculate $\mathcal{A}$-subproblem, there has a total complexity $\mathcal{O}(S \cdot \max\{W^2 H^2, \log S\})$ for each iteration [71]. For $\mathcal{B}$-subproblem, there needs to compute the t- SVD of the tensor with the size of $r \times W \times H$, thus the complexity to $\mathcal{B}$-subproblem is $\mathcal{O}(H \cdot \min\{W^2 r, r^2 W\})$ for each iteration. For $\mathcal{C}$-subproblem (25), the most heavy step is updating $\mathcal{N}$ by (30), where requires computing a t-SVD of J tensor with the size of $r \times d_i \times q^2$, $i = 1, \cdots, J$. Thus, the complexity of $\mathcal{C}$-subproblem is $\mathcal{O}(q^2 \sum_{i=1}^{J} \min\{d_i^2 r, r^2 d_i\})$ for each iteration in Algorithm 1. Let E_1, E_2, and E_3 denotes the number of iterations in Algorithm 1, Algorithm 2 and Algorithm 3, respectively. The total complexity of Algorithm 3 is $\mathcal{O}(E_3 \cdot (E_2 \cdot (S \cdot \max\{W^2 H^2, \log S\} + H \cdot \min\{W^2 r, r^2 W\} + E_1 \cdot q^2 \sum_{i=1}^{J} \min\{d_i^2 r, r^2 d_i\})))$.

IV. EXPERIMENTS

To verify the effectiveness of the proposed IR-TenSR method, we test it on three simulated datasets and one real dataset. Meanwhile, we compare the proposed IR-TenSR with seven state-of-the-art HSI-SR approaches to demonstrate its superiority, including MatSR-based methods (HySure [53] and LTMR [61]), nonnegative matrix factorization method CNMF [48], nonlocal TF-based approaches (LTMR [61], NLSTF [35], and LTTR [44]), TF-based CSTF [37], and sparse representation-based S^4-LRR [30]. We download all approaches' codes from the authors' homepages and tune parameters to the best outputs according to the reference commendations. Our parameters are discussed in detail in Section V-B. We perform all experiments in MATLAB R2020a on an Intel(R) Core(TM) i9-10900KF CPU @ 3.70GHz 64.00GB RAM platform.

A. Datasets

This part introduces four datasets for experiments, including three simulated datasets and one real dataset.

Algorithm 3 Iterative Regularization Algorithm.

Input: Permuted HSI $\mathcal{Y}_4$, Permuted MSI $\mathcal{Z}_4$.
Initialize: $\mathcal{Y}_4^0 = \mathcal{Y}_4$, $\mathcal{Z}_4^0 = \mathcal{Z}_4$.
1: **for** $\tau = 0 \to E_3 - 1$ **do**
2:      Update $\mathcal{X}_4^{\tau+1}$ by Algorithm 2.
3:      Generate $\widehat{\mathcal{Y}_4}$ and $\widehat{\mathcal{Z}_4}$ by (16).
4:      Generate $\mathcal{Y}_4^{\tau+1} = \mathcal{Y}_4^\tau - \widehat{\mathcal{Y}_4}$, $\mathcal{Z}^{\tau+1} = \mathcal{Z}_4^\tau - \widehat{\mathcal{Z}_4}$.
5: **end for**
Output: $\mathcal{X} = \text{ipermute}(\sum_{\tau=1}^{E_3} \mathcal{X}_4^\tau, [1,3,2])$.

---

1) Simulated Datasets:

- The first simulated dataset is Pavia University of size $610 \times 340 \times 115$ [72]. We retain 93 bands by removing the low signal-to-noise ratio (SNR) bands and choose the up-left 256×256 cube as ground truth (GT), i.e., $S = 93$, $W = 256$, $H = 256$. We generate the HSI by uniform blur of ratio 16, i.e., $w = W/16 = 16$, $h = H/16 = 16$. We obtain the MSI with four bands by the IKONOS-like reflectance spectral response filter, i.e., $s = 4$.

- The second one is Indian Pines of size $145 \times 145 \times 220$ [73]. We remove the bands with a low SNR, 182 bands are retained. We choose the up-left 128×128 cube as GT, i.e., $S = 182$, $W = 128$, $H = 128$. We obtain the HSI by uniform blur of ratio 4, i.e., $w = W/4 = 32$, $h = H/4 = 32$. We generate the MSI with six bands by Landsat7-like spectral response, i.e., $s = 6$.

- The third one is the Harvard with fifty HSIs, describing outdoor and indoor scenes under daylight illumination [65]. Each of HSIs has 31 spectral bands and of spatial resolution 1392×1040. Three HSIs (i.e, imgb0, imgb9, and imge1) are randomly chosen, then select the up-left 512×512 cube of each of selected HSIs as GT, i.e., $S = 31$, $W = 512$, $H = 512$. The HSI is obtained by uniform blur of ratio 16, i.e., $w = W/16 = 32$, $h = H/4 = 32$. Besides, we obtain the MSI with three bands by the Nikon D700 camera, i.e., $s = 3$.

When we generate the HSI and MSI of the above three datasets, respectively, the Gaussian noise with the same SNR is simultaneously added to MSI and HSI, where SNR is varied between 10 and 25 dB, with an interval of 5 dB.

2) Real Dataset:

- The acquired HSI [11] has 220 spectral bands in the spectral range of 400-2500nm and spatial resolution of 30m obtained by the Hyperion sensor loaded on the Earth-Observing-1 satellite. We retain 89 bands by removing the low SNR bands and choose space of size 80×80 to simulate HSI, i.e., $w = 80$, $h = 80$, $S = 89$. The MSI with thirteen spectral bands is obtained by the Sentinel-2A satellite, and we select four bands with the spatial size of 240×240 to simulate MSI, i.e., $W = 240$, $H = 240$, $s = 4$. The central wavelengths of the four bands are 490, 560, 665, and 842 nm.

B. Evaluation Index

For a given GT $\mathcal{X} \in \mathbb{R}^{J_1 \times J_2 \times J_3}$ and the fused results $\widehat{\mathcal{X}} \in \mathbb{R}^{J_1 \times J_2 \times J_3}$, we introduce the following five evaluation indexes

to assess the quality of $\widehat{\mathcal{X}}$.

- The peak signal to noise ration (PSNR) [38].

$$\text{PSNR}(\mathcal{X}, \widehat{\mathcal{X}}) = \frac{1}{J_3} \sum_{i=1}^{J_3} \text{PSNR}(\mathbf{X}_i, \widehat{\mathbf{X}}_i),$$

where $\mathbf{X}_i$ ($\mathbf{X}_i \in \mathbb{R}^{J_1 \times J_2}$) and $\widehat{\mathbf{X}}_i$ ($\widehat{\mathbf{X}}_i \in \mathbb{R}^{J_1 \times J_2}$) are the i-th ($i = 1, 2, \cdots, J_3$) band of $\mathcal{X}$ and $\widehat{\mathcal{X}}$, respectively.

- The root means square error (RMSE) [38].

$$\text{RMSE}(\mathcal{X}, \widehat{\mathcal{X}}) = \sqrt{\frac{||\mathcal{X} - \widehat{\mathcal{X}}||_F^2}{J_1 J_2 J_3}},$$

which evaluates the estimation error between $\mathcal{X}$ and $\widehat{\mathcal{X}}$. The best value is 0.

- The structure similarity (SSIM) [74].

$$\text{SSIM}(\mathcal{X}, \widehat{\mathcal{X}}) = \frac{1}{J_3} \sum_{i=1}^{J_3} \text{SSIM}(\mathbf{X}_i, \widehat{\mathbf{X}}_i),$$

which evaluates the structure similarity between $\mathcal{X}$ and $\widehat{\mathcal{X}}$. The best value is 1.

- The relative dimensionaless global error in synthesis (ERGAS) [38].

$$\text{ERGAS}(\mathcal{X}, \widehat{\mathcal{X}}) = \frac{100}{d} \sqrt{\frac{1}{J_3} \sum_{i=1}^{J_3} \frac{\text{MSE}(\mathbf{X}_i, \widehat{\mathbf{X}}_i)}{\mu_{(\widehat{\mathbf{X}}_i)}^2}},$$

which evaluates the quality of $\widehat{\mathcal{X}}$. The best value is 0.

- The spectral angle mapper (SAM) [38].

$$\text{SAM}(\mathcal{X}, \widehat{\mathcal{X}}) = \frac{1}{J_1 J_2} \sum_{i=1}^{J_1 J_2} \text{arcos} \frac{\widehat{\mathbf{x}_j}^T \mathbf{x}_j}{||\widehat{\mathbf{x}_j}||_2 ||\mathbf{x}_j||_2},$$

where $\widehat{\mathbf{x}_j} \in \mathbb{R}^{J_3}$ and $\mathbf{x}_j \in \mathbb{R}^{J_3}$ ($j = 1, 2, \cdots, J_1 J_2$) are pixels in $\mathcal{X}$ and $\widehat{\mathcal{X}}$, respectively. SAM is given in degrees and the best value is 0.

C. Experiments Results on Three Simulated Datasets

1) Results on Pavia University Dataset: Table I presents the evaluation indexes comparison of all methods on the Pavia University dataset under different noise levels. We highlight the optimal and suboptimal results in bold and underlined, respectively. From the table, the nonnegative matrix factorization method CNMF and nonlocal TF-based method LTTR have poor outputs compared with MatSR-based methods, HySure and LTMR. NLSTF and CSTF obtain satisfactory results in all noise levels. S^4-LRR generates beautiful outputs in low SNR cases, which means the sensitivity to noise. The proposed IR-TenSR has competitive performance in all SNR cases. For example, when SNR is 15, the PSNR of the image reconstructed by the proposed IR-TenSR is more than 7 dB higher than that of the suboptimal LTMR. The reasons include 1) we exploit the TenSR to represent the target HR-HSI, the smaller subspace dimension (the lower tubal rank) can help to keep the noise out; 2) we consider the spatial-spectral nonlocal self-similarity property of the

target HR-HSI, and 3) we utilize the residual information of acquired low-resolution images.

For visual comparison, the fused results consisted of the 10-th band, 16-th band, and 47-th band of the fused images under SNR=25dB, and the corresponding error results are presented in Fig. 5. We magnify the representative region (denoted by red block). As shown in the magnified regions and error outputs, the reconstructed images by CNMF and NLSTF exist noise; S^4-LRR and HySure have apparent flaws; images fused by CSTF, LTMR, and LTTR generate good results, but the details cannot be better preserved. By concentrating on the spatial-spectral nonlocal self-similarity property and spatial-spectral correlation property, combined with residual information, the proposed IR-TenSR obtains the best-fused output, preserving most of the details and removing noises. From the error image, the HR-HSI produced by the proposed IR-TenSR has fewer errors than that of other compared approaches.

2) Results on Indian Pines Dataset: We present the evaluation indexes comparison of all approaches on the Indian Pines dataset in Table II. We highlight the optimal and suboptimal results in bold and underlined, respectively. From the table, the nonlocal TF-based method LTTR has poor outputs compared with MatSR-based methods, HySure and LTMR. NLSTF and CSTF obtain satisfactory results in all noise levels. CNMF and S^4-LRR get beautiful outputs in high SNR cases. In general, the proposed IR-TenSR has better performance. For example, when SNR is 10, the RMSE of the image reconstructed by the proposed IR-TenSR is 2.23 lower than that of the suboptimal HySure. For visual comparison, we show the outputs consisted of the reconstructed 11-th band, 48-th band, and 128-th band of the fused images under SNR=15dB, and the corresponding error maps in Fig. 6. We magnify the representative region (denoted by blue block). As shown in the magnified regions and error outputs, the reconstructed images by CNMF, HySure, CSTF, NLSTF, LTTR, LTMR, and S^4-LRR exist noise; CNMF, HySure, LTTR, and S^4-LRR have apparent flaws. The proposed IR-TenSR obtains the best-fused output and removes most of the noises contained in images. From the error images, we find that the HR-HSI produced by the proposed IR-TenSR has fewer errors than that of other compared approaches.

3) Results on Harvard Dataset: There are 12 experiments in the Harvard dataset since we choose three HSIs with four different SNR cases. Table III shows the evaluation indexes comparison of all methods on three HSIs under four noise levels. We highlight the optimal and suboptimal results in bold and underlined, respectively. From the table, LTTR and CNMF have poor outputs compared with MatSR-based methods, HySure and LTMR. NLSTF and CSTF generate satisfactory results in all noise cases. S^4-LRR obtains beautiful outputs in high SNR cases. The proposed IR-TenSR has better performance than other compared methods. For example, when SNR is 10, the SSIM of imgb0 reconstructed by the proposed IR-TenSR

is 0.31 higher than HySure. For visual comparison, the outcomes consisted of the reconstructed 6-th band, 15-th band, and 28-th band of the fused imgb9 under SNR=15dB, and the corresponding error maps are shown in Fig. 7. We magnify the representative region (denoted by red block). As shown in the magnified regions and error outputs, the reconstructed images by CNMF, NL-STF, LTTR, S⁴-LRR, and LTMR exist apparent noise and flaws; HySure and CSTF produce better results but have less noise. In contrast, our method obtains the best-fused result; the HR-HSI made by the proposed IR-TenSR has fewer errors than that of other compared approaches, as shown in the error images.

TABLE I
QUANTITATIVE EVALUATION OF DIFFERENT METHODS ON PAVIA
UNIVERSITY DATASET WITH FOUR NOISE CASES

Evaluation Index	PSNR	SSIM	ERGAS	SAM	RMSE
Best Value	$+\infty$	1	0	0	0
SNR=25dB					
CNMF [48]	28.88	0.81	1.35	6.79	9.38
HySure [53]	31.59	0.93	1.00	5.69	6.83
CSTF [37]	37.29	0.95	0.50	3.51	3.57
NLSTF [35]	37.59	0.96	0.48	3.41	3.46
LTTR [44]	35.31	0.94	0.67	4.21	4.84
LTMR [61]	38.24	0.96	0.45	**3.15**	3.21
S⁴-LRR [30]	34.84	0.95	0.70	4.29	4.81
IR-TenSR	**40.98**	**0.98**	**0.41**	3.26	**3.02**
SNR=20dB					
CNMF [48]	27.55	0.74	1.52	9.82	11.08
HySure [53]	30.91	0.91	1.06	6.07	7.40
CSTF [37]	34.38	0.90	0.70	4.69	4.99
NLSTF [35]	33.78	0.89	0.75	5.22	5.35
LTTR [44]	33.24	0.90	0.82	5.45	5.76
LTMR [61]	35.33	0.92	0.62	4.14	4.46
S⁴-LRR [30]	32.25	0.90	0.92	5.51	6.45
IR-TenSR	**40.20**	**0.97**	**0.44**	**3.52**	**3.18**
SNR=15dB					
CNMF [48]	23.53	0.53	2.44	16.92	17.55
HySure [53]	29.28	0.83	1.26	7.02	8.97
CSTF [37]	30.67	0.79	1.06	6.82	7.71
NLSTF [35]	29.05	0.73	1.30	8.87	9.26
LTTR [44]	29.43	0.78	1.29	9.03	8.66
LTMR [61]	30.99	0.79	1.04	6.77	7.35
S⁴-LRR [30]	29.35	0.79	1.25	7.30	8.97
IR-TenSR	**38.29**	**0.96**	**0.50**	**4.17**	**3.61**
SNR=10dB					
CNMF [48]	23.58	0.51	2.39	15.39	17.64
HySure [53]	26.34	0.67	1.74	9.20	12.72
CSTF [37]	26.93	0.63	1.62	9.75	12.01
NLSTF [35]	24.02	0.50	2.34	15.50	16.70
LTTR [44]	23.58	0.53	2.57	17.93	17.25
LTMR [61]	25.39	0.55	2.00	12.9	14.26
S⁴-LRR [30]	26.43	0.64	1.74	9.73	12.46
IR-TenSR	**32.23**	**0.89**	**0.92**	**7.92**	**6.47**

D. Experiments Results on Real Dataset

We perform the proposed approach on real dataset mentioned in Section IV-A to further evaluate its performance. To simulated MSI and HSI, we estimate spatial blurring kernel $\mathbf{B}$ and spectral response matrix $\mathbf{R}$ via work [53]. Specifically, we have $\mathbf{RY}_{(3)} = \mathbf{Z}_{(3)}\mathbf{BS}$ based on formulations (8) and (10). Thus, we estimate $\mathbf{B}$ and $\mathbf{S}$ by problem $\operatorname{argmin}_{\mathbf{B},\mathbf{S}} ||\mathbf{RY}_{(3)} - \mathbf{Z}_{(3)}\mathbf{BS}||_F^2 + \lambda_b\Phi_b(\mathbf{B}) +$

TABLE II
QUANTITATIVE EVALUATION OF DIFFERENT METHODS ON INDIAN PINES
DATASET WITH FOUR NOISE CASES

Evaluation Index	PSNR	SSIM	ERGAS	SAM	RMSE
Best Value	$+\infty$	1	0	0	0
SNR=25dB					
CNMF [48]	30.12	0.83	2.30	4.28	9.05
HySure [53]	28.73	0.84	2.77	4.97	10.58
CSTF [37]	**30.76**	**0.85**	**2.24**	4.26	**8.86**
NLSTF [35]	29.39	0.84	2.54	4.49	9.87
LTTR [44]	25.27	0.67	4.05	6.54	14.75
LTMR [61]	27.67	0.82	3.01	4.99	11.37
S⁴-LRR [30]	30.28	0.83	2.31	4.38	8.91
IR-TenSR	30.24	0.83	2.40	**4.17**	9.39
SNR=20dB					
CNMF [48]	27.60	0.76	2.92	5.04	11.42
HySure [53]	28.31	**0.83**	2.86	5.05	10.95
CSTF [37]	29.07	0.80	2.57	4.65	10.06
NLSTF [35]	28.25	0.80	2.81	4.96	10.96
LTTR [44]	23.32	0.56	5.01	8.55	17.93
LTMR [61]	27.13	0.78	3.18	5.33	12.03
S⁴-LRR [30]	23.56	0.56	5.63	9.17	18.61
IR-TenSR	**30.05**	**0.83**	2.46	**4.25**	**9.44**
SNR=15dB					
CNMF [48]	24.31	0.61	4.21	6.71	16.29
HySure [53]	27.31	**0.78**	3.11	5.30	12.00
CSTF [37]	25.74	0.65	3.57	6.00	14.02
NLSTF [35]	25.51	0.69	3.71	6.42	14.34
LTTR [44]	20.04	0.40	7.45	13.03	26.14
LTMR [61]	24.27	0.60	4.36	7.47	16.75
S⁴-LRR [30]	20.10	0.39	7.84	13.43	26.69
IR-TenSR	**28.74**	**0.78**	**2.73**	**4.86**	**10.39**
SNR=10dB					
CNMF [48]	19.85	0.38	6.88	10.66	26.82
HySure [53]	25.27	**0.68**	3.78	**5.92**	14.68
CSTF [37]	19.91	0.37	6.84	11.24	26.74
NLSTF [35]	20.77	0.45	6.31	10.75	23.98
LTTR [44]	15.83	0.22	11.77	20.63	42.06
LTMR [61]	18.86	0.33	8.07	13.78	31.57
S⁴-LRR [30]	15.98	0.22	11.72	20.55	41.63
IR-TenSR	**26.74**	**0.68**	**3.32**	6.02	**12.45**

$\lambda_r\Phi_r(\mathbf{R})$, where $\Phi_b(\cdot)$ and $\Phi_r(\cdot)$ denotes the regularizer of $\mathbf{B}$ and $\mathbf{R}$, respectively, λ_b and λ_r are regularization parameters. $\Phi_b(\mathbf{B})$ is set to $||\mathbf{D}_h\mathbf{B}||_F^2 + ||\mathbf{D}_v\mathbf{B}||_F^2$, where $\mathbf{D}_h$ and $\mathbf{D}_v$ are the difference operator along the horizontal and vertical direction, respectively. Since we only need to smooth $\mathbf{R}$ along the vertical direction, $\Phi_r(\mathbf{R})$ is set to $||\mathbf{D}_v\mathbf{R}||_F^2$. We first estimate $\mathbf{R}$ and then obtain $\mathbf{B}$ with known $\mathbf{R}$.

Fig. 8 presents the results consisting of 1-st band, 88-th band, and 89-th band of the fused images. The MSI shown in Fig. 8 consists of 1-st, 2-nd, and 4-th bands of the original MSI mentioned in Section IV-A. We magnify the representative region (denoted by blur block). We find that fused images by LTTR and S⁴-LRR have serious spectral distortion since there is an obvious color change. Besides, compared with the shown MSI, we find that the fused images by CNMF, CSTF, and NLSTF cannot recover the spatial structure well, as shown in the enlarged blue boxes. In contrast, though the reconstructed image by the proposed IR-TenSR is imperfect, it makes a balance between spectral distortion and spatial structure retaining.

TABLE III
QUANTITATIVE EVALUATION OF DIFFERENT METHODS ON THREE HSIS OF HARVARD DATASET WITH FOUR NOISE CASES

Method	imgb0					imgb9					imge1				
	PSNR	SSIM	ERGAS	SAM	RMSE	PSNR	SSIM	ERGAS	SAM	RMSE	PSNR	SSIM	ERGAS	SAM	RMSE
	SNR=25dB					SNR=25dB					SNR=25dB				
CNMF [48]	34.70	0.87	1.09	6.54	5.29	34.25	0.80	1.27	7.32	5.57	24.75	0.59	1.45	12.27	16.24
HySure [53]	37.43	0.94	0.76	4.50	4.16	39.68	0.94	0.74	4.18	2.87	24.16	0.63	1.53	11.60	17.83
CSTF [37]	40.12	0.95	0.57	3.65	3.11	42.73	0.95	0.52	3.30	2.03	25.87	0.75	1.24	8.61	14.51
NLSTF [35]	38.15	0.92	0.92	5.53	3.54	41.28	0.93	0.65	4.20	2.34	25.05	0.57	1.47	16.77	15.44
LTTR [44]	36.17	0.89	1.33	5.95	4.09	39.62	0.91	0.89	5.33	2.75	24.88	0.55	1.56	17.99	15.45
LTMR [61]	38.98	0.93	0.77	4.30	3.13	42.02	0.94	0.62	3.85	2.12	25.20	0.58	1.52	14.93	14.96
S^4-LRR [30]	39.13	0.94	0.65	5.03	3.36	40.94	0.94	0.66	4.41	2.45	25.63	0.63	1.30	13.46	14.78
IR-TenSR	42.70	0.98	0.63	2.60	2.12	44.38	0.98	0.49	2.88	1.64	26.55	0.83	1.16	7.70	13.38
	SNR=20dB					SNR=20dB					SNR=20dB				
CNMF [48]	33.05	0.81	1.43	8.65	6.17	31.23	0.67	1.93	12.44	7.60	23.64	0.44	1.96	19.6	17.70
HySure [53]	34.93	0.89	1.04	5.38	5.32	37.10	0.88	0.98	5.22	3.82	22.93	0.43	1.82	15.35	20.45
CSTF [37]	36.46	0.88	0.85	5.24	4.74	38.71	0.89	0.82	4.97	3.18	25.42	0.62	1.31	11.14	15.27
NLSTF [35]	32.73	0.78	1.77	9.09	6.30	35.93	0.82	1.29	7.93	4.25	23.17	0.38	1.94	21.94	18.80
LTTR [44]	30.87	0.74	2.47	10.57	7.52	34.31	0.78	1.67	9.75	5.08	22.35	0.35	2.33	24.43	20.14
LTMR [61]	33.77	0.80	1.41	7.65	5.82	37.21	0.85	1.09	6.71	3.74	23.38	0.38	2.04	21.76	18.88
S^4-LRR [30]	35.65	0.87	0.96	6.35	4.81	37.77	0.76	0.92	5.87	3.54	22.98	0.37	2.03	22.50	18.99
IR-TenSR	41.63	0.97	0.75	2.92	2.32	43.62	0.97	0.56	3.16	1.77	26.35	0.81	1.21	9.24	13.56
	SNR=15dB					SNR=15dB					SNR=15dB				
CNMF [48]	25.50	0.50	3.17	17.42	14.93	29.84	0.57	2.53	15.65	8.70	19.86	0.23	3.04	28.00	27.20
HySure [53]	30.30	0.73	1.93	9.31	9.20	32.34	0.69	1.78	9.00	6.59	20.85	0.28	2.45	19.08	26.15
CSTF [37]	29.47	0.63	2.08	13.55	11.77	33.24	0.70	1.61	9.79	5.96	23.89	0.41	1.56	17.46	18.20
NLSTF [35]	26.35	0.51	3.96	15.81	12.90	29.76	0.56	2.71	15.28	8.62	19.52	0.18	3.41	27.85	27.86
LTTR [44]	25.51	0.51	4.54	17.60	13.94	28.97	0.55	3.07	17.19	9.37	18.89	0.20	3.75	30.23	29.64
LTMR [61]	27.23	0.52	3.65	15.62	13.10	31.25	0.61	2.13	13.13	7.58	19.64	0.19	3.50	28.73	29.24
S^4-LRR [30]	26.62	0.53	3.69	15.66	12.48	33.50	0.71	1.48	8.96	5.82	18.62	0.19	3.85	29.88	30.57
IR-TenSR	39.75	0.96	0.96	3.62	2.79	42.15	0.96	0.69	3.75	2.07	25.98	0.76	1.30	11.55	13.96
	SNR=10dB					SNR=10dB					SNR=10dB				
CNMF [48]	20.06	0.26	6.54	27.70	27.29	22.30	0.24	5.47	30.85	21.2	15.48	0.10	4.95	32.58	44.83
HySure [53]	28.61	0.61	2.01	8.27	11.54	27.13	0.43	3.24	16.77	13.00	21.43	0.27	2.10	15.26	24.46
CSTF [37]	22.00	0.28	6.05	25.69	28.36	27.91	0.43	3.02	18.11	11.41	20.83	0.23	2.43	24.19	25.67
NLSTF [35]	21.09	0.26	7.27	24.12	23.67	23.92	0.29	5.37	24.99	16.89	15.36	0.10	5.88	33.80	44.80
LTTR [44]	20.58	0.29	8.07	26.68	24.60	23.63	0.30	5.71	27.92	17.28	14.93	0.11	6.20	35.73	46.57
LTMR [61]	19.57	0.21	11.95	30.54	33.49	25.85	0.35	4.02	22.47	14.24	15.35	0.10	6.13	35.09	47.73
S^4-LRR [30]	20.73	0.28	7.89	25.74	24.22	24.51	0.31	4.92	25.76	15.81	14.27	0.10	7.06	35.82	49.87
IR-TenSR	36.78	0.92	1.38	5.09	3.83	39.54	0.94	0.97	5.05	2.76	25.25	0.66	1.49	15.05	14.89

CNMF [48] HySure [53] CSTF [37] NLSTF [35] LTTR [44] LTMR [61] S^4-LRR [30] IR-TenSR Ground Truth
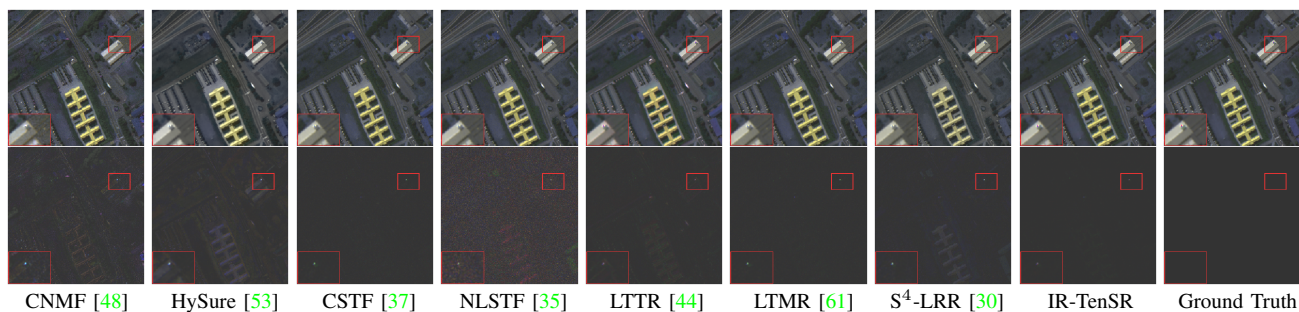
Fig. 5. HSI-SR results of Pavia University. The first row and second row present the outcomes consisting of 10-th, 16-th, 47-th bands of the fused images under SNR=25dB and the corresponding error results, respectively. The red block shows the representation region.

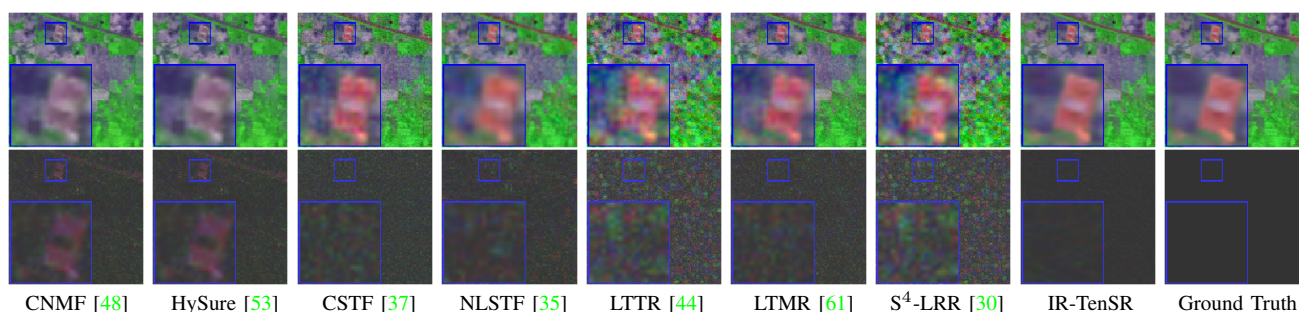CNMF [48] HySure [53] CSTF [37] NLSTF [35] LTTR [44] LTMR [61] S^4-LRR [30] IR-TenSR Ground Truth

Fig. 6. HSI-SR results of Indian Pines. The first row and second row present the results consisting of 11-th, 48-th, 128-th band of the fused images under SNR=15dB and the corresponding error maps, respectively. The blue block shows the representation region.
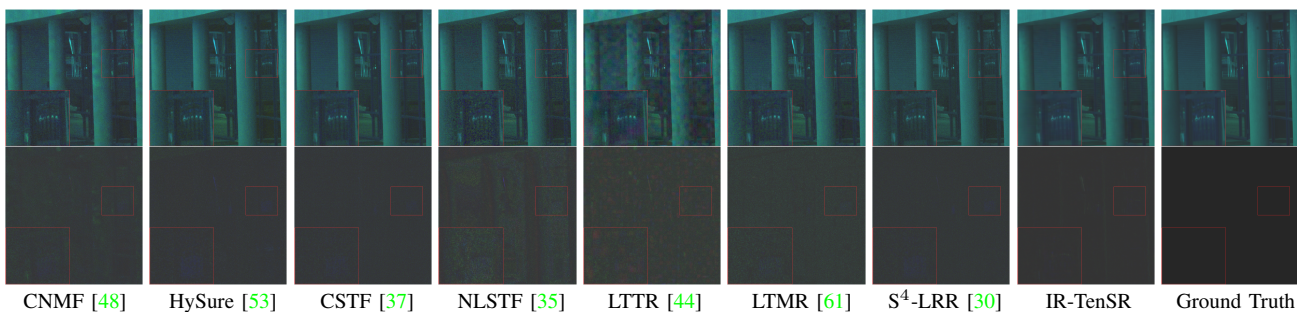
Fig. 7. HSI-SR results of imgb9 (an HSI in Harvard DATASET). The first row and second row present the results consisting of 1-th, 15-th, 31-th band of the fused images under SNR=15dB and the corresponding error outputs, respectively. The red block shows the representation region.
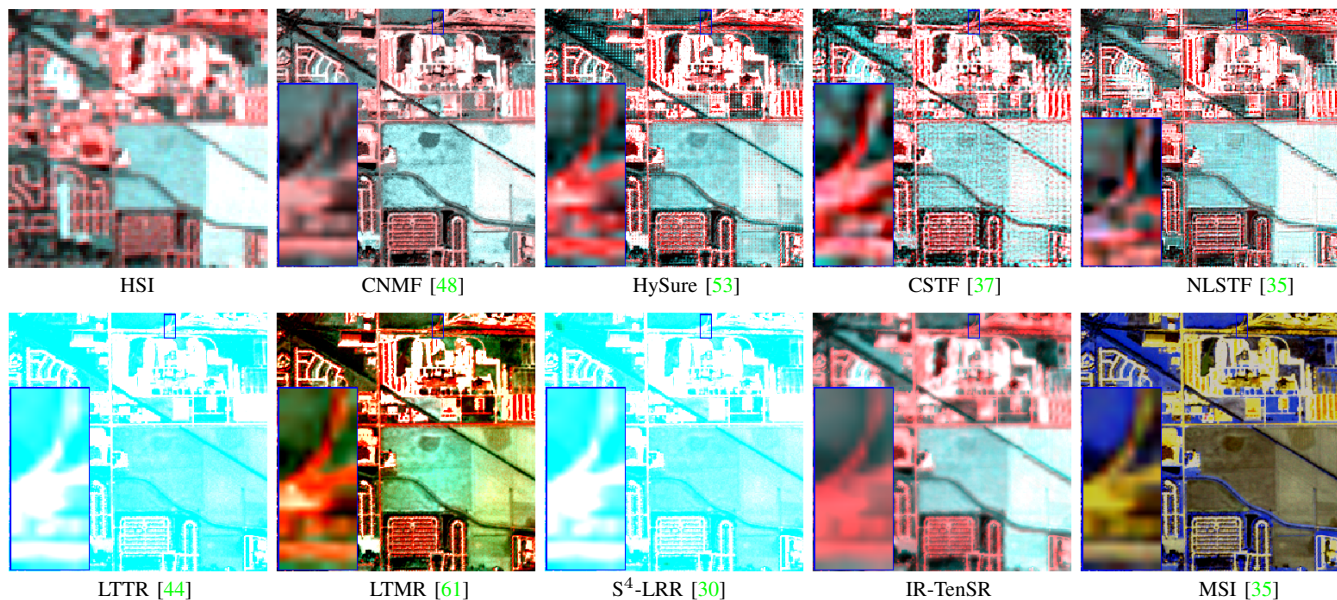

Fig. 8. HSI-SR results of real data. This figure presents the results consisting of 1-st, 88-th, and 89-th bands of the fused image. The MSI consists of 1-st, 2-nd, 4-th bands of the original MSI. The blue block shows the representation region.

V. DISCUSSION

A. Determination of the Permuted Tensor

As mentioned in Section III-A2, tensor whose spectral dimension is in mode-1 or mode-2 has a lower tubal rank. Thus, we test them (i.e., $\mathcal{X}_2$, $\mathcal{X}_3$, $\mathcal{X}_4$, and $\mathcal{X}_5$) on the Indian Pines dataset, Harvard dataset, and Pavia University dataset to determine which one is more favorable for the fusion results. Fig. 9 shows the curve of PSNR and SAM of the fusion results on three datasets under four different permuted tensors. From Fig. 9, it is not difficult to find that the performance of the two evaluation indexes (i.e., PSNR and SAM) is the best in the case of $\mathcal{X}_4$. Therefore, we chose permuted tensor $\mathcal{X}_4$ for all of our experiments.

B. Parameters Analyses

There are seven parameters in the proposed IR-TenSR, including proximal parameter β, penalty parameter γ, regularization parameter λ, positive hyper-parameter μ, 3-D block number Λ and size q, and tubal-rank r. For simulated datasets, we choose the parameter with the best PSNR and SAM value
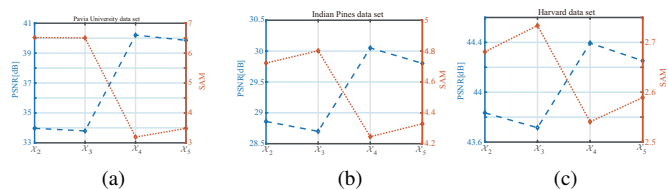

Fig. 9. Statistical analysis of the effectiveness of four permuted tensors (i.e., $\mathcal{X}_2$, $\mathcal{X}_3$, $\mathcal{X}_4$, and $\mathcal{X}_5$) on three simulated datasets.

as the parameter of the dataset; for real dataset, we choose the parameters with a good visual effect.

1) Simulated data sets: Parameter μ denotes a positive hyper-parameter to promote $\mathcal{A}$ to be closed to $\mathcal{B} * \mathcal{C}$. To analyze μ, we perform the proposed algorithm for different μ on the Pavia University dataset. Fig. 10 (a) presents PSNR and SAM curves concerning different μ. In the experiment, we set μ to $[10^{-7}, 10^{-3}]$. The SAM decreases when μ varies from 10^{-7} to 10^{-4} and increases from 10^{-4} to 10^{-3}; the PSNR increases when μ varies from 10^{-7} to 10^{-4} and decreases from 10^{-4} to 10^{-3}, thus, we set μ as 10^{-4}. Similarly, we set

μ as 5×10^{-7} and 10^{-6} for Indian Pines and Harvard dataset, respectively.

To analyze the influence of β, we perform the proposed algorithm with different β on Pavia University dataset. Fig. 10 (b) presents PSNR and SAM curves concerning different β. In the experiment, we set β to $[10^{-7}, 10^{-3}]$. The SAM fluctuates slightly when β varies from 10^{-7} to 10^{-5} and increases from 10^{-5} to 10^{-3}; the PSNR fluctuates slightly when β varies from 10^{-7} to 10^{-5} and decreases from 10^{-5} to 10^{-3}, thus, we set β as 5×10^{-7}. Similarly, we set β to 10^{-5} and 5×10^{-5} for Indian Pines and Harvard dataset, respectively.

To analyze γ, we perform the proposed algorithm for different γ on Pavia University dataset. Fig. 10 (c) presents PSNR and SAM curves concerning different γ. In the experiment, we set γ to $[10^{-5}, 10^{-1}]$. The SAM fluctuates slightly when γ varies from 10^{-5} to 10^{-3} and decreases from 10^{-3} to 10^{-1}; the PSNR remains stable when γ varies from 10^{-5} to 10^{-3} and increases from 10^{-3} to 10^{-1}, thus, we set γ as 10^{-1}. Similarly, we set γ as 10^{-5} and 10^{-3} for Indian Pines and Harvard dataset, respectively.

To analyze λ, we perform the proposed algorithm for different λ on Pavia University dataset. Fig. 10 (d) presents PSNR and SAM curves concerning different λ. In the experiment, we set λ to $[5 \times 10^{-7}, 5 \times 10^{-3}]$. The SAM fluctuates slightly when λ varies from 5×10^{-7} to 5×10^{-5} and increases from 5×10^{-5} to 5×10^{-3}; the PSNR remains stable when λ varies from 5×10^{-7} to 5×10^{-5} and increases from 5×10^{-5} to 5×10^{-3}, thus, we set λ as 5×10^{-3}. Similarly, we set λ as 10^{-7} and 10^{-4} for Indian Pines and Harvard dataset, respectively.

To analyze Λ, we perform the proposed algorithm for different Λ on the Pavia University dataset. Fig. 10 (e) presents PSNR and SAM curves concerning different Λ. In the experiment, we set Λ to $[2, 42]$. The SAM increases when Λ varies from 2 to 42; the PSNR decreases when Λ varies from 2 to 42, thus, we set Λ as 2. Similarly, we set Λ as 32 and 22 for Indian Pines and Harvard dataset.

To analyze patch size q, we perform the proposed algorithm for different q on the Pavia University dataset. Fig. 10 (f) presents PSNR and SAM curves concerning different q. In the experiment, we set q to $[7, 21]$. The SAM decreases when q varies from 7 to 21; the PSNR increases when q varies from 7 to 21, thus, we set q as 21. Similarly, we set q as 9 and 7 for Indian Pines and Harvard datasets.

To analyze the dimension of TenSR r, we run the proposed algorithm for different r on the Pavia University dataset. Fig. 10 (g) presents PSNR and SAM curves concerning different r. In the experiment, we set r to $[2, 11]$. The SAM increases when r varies from 2 to 8 and waves from 8 to 11; the PSNR increases when r varies from 2 to 4 and decreases from 4 to 11, thus, we set r as 3. Similarly, we set r as 8 and 11 for Indian Pines and Harvard datasets.

We summarize the ranges and values of all parameters used in three simulated datasets in Table IV.

2) Real datatset: Similar to the strategy of determining the parameters of the three simulated datasets, we select the parameters of the real data set. We choose them according to the visual effect rather than the evaluation index, i.e., PSNR

and SAM. For brevity, we summarize the parameters used in the real data set in Table IV.
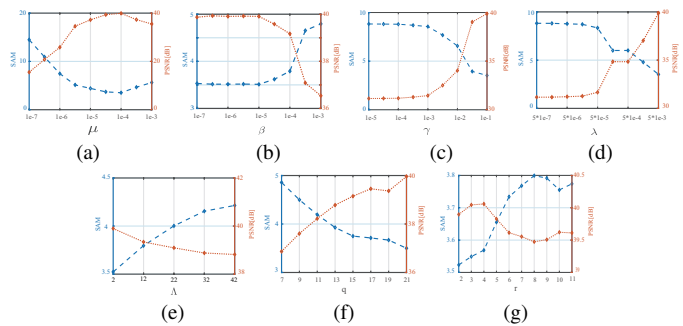

Fig. 10. Sensitivity analysis of parameters on the Pavia University dataset.

C. Analysis of the Iterative Regularization Algorithm

In Section III-C, we design an iterative regularization procedure to exploit the residual information of the acquired low-resolution images. This section will verify its effectiveness and determine the number of iterations E_3 in Algorithm 3. Fig.11 presents the change of PSNR and time concerning different τ on the three datasets, i.e., (a) Pavia University dataset, (b) Indian Pines dataset, and (c) Harvard dataset. When τ is from 1 to 3, the PSNR of the results obtained by Algorithm 3 increases significantly, which shows the effectiveness of the designed iterative regularization procedure. When τ is greater than 3, the PSNR curve tends to be flat. To sum up, we set the maximum iteration steps E_3 as 6, 7, and 3 for Pavia University, Indian Pines, and Harvard dataset, respectively.
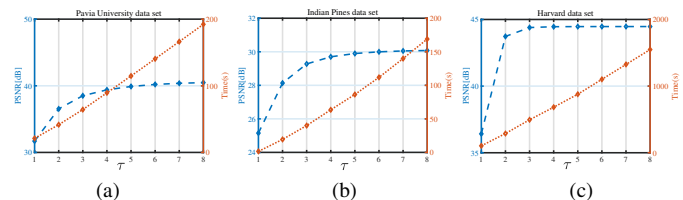

Fig. 11. Influence of the number of outer iterations τ on the fusion effect and efficiency.

D. Analysis of the Regularization Term

In this part, we discuss the performance of the regularization term (i.e., $\mathcal{J}(\mathcal{C})$) in model (18). Specifically, we perform the following two points:

- Ponit-1. Set λ in Eq. (18) as zero, then test the model on three simulated datasets mentioned in Section IV-A, and compare with the proposed model with $\lambda \neq 0$;
- Point-2. Impose the matrix nuclear norm (MNN) on matrix $(\mathcal{U}_i\mathcal{C})_{(2)}$, $i = 1, \cdots, CC$, rather than tensor nuclear norm (TNN) on $\mathcal{U}_i\mathcal{C}$ to character the spatial-spectral nonlocal self-similarity property of tensor coefficient $\mathcal{C}$.

For point 1, we aim to illustrate the effectiveness of the regularization term. For point 2, we want to present that it is more effective to impose TNN on tensors $\mathcal{U}_i\mathcal{C}$ than

TABLE IV
PARAMETERS DISCUSSION OF THE PROPOSED METHOD ON THREE SIMULATED DATASETS AND ONE REAL DATASET.

Parameter	β	γ	λ	μ	Λ	q	r
			Simulated datasets				
Suggested Range	$[10^{-7}, 10^{-3}]$	$[10^{-5}, 10^{-1}]$	$[5 \times 10^{-7}, 5 \times 10^{-3}]$	$[10^{-7}, 10^{-3}]$	$[2, 42]$	$[7, 21]$	$[2, 11]$
Pavia University [72]	5×10^{-7}	10^{-1}	$5 * 10^{-3}$	10^{-4}	2	21	3
Indian Pines [73]	10^{-5}	10^{-5}	10^{-7}	5×10^{-7}	32	9	8
Harvard [65]	5×10^{-5}	10^{-3}	10^{-4}	10^{-6}	22	7	11
			Real datasets				
Real data [11]	10^{-7}	10^{-5}	$5 * 10^{-7}$	$5 * 10^{1}$	10	7	5

MNN used in [59] to character the spatial-spectral nonlocal self-similarity property. Table V and Table VI present the quantitative analysis results of these two points. From Table V, we find that the regularization term is effective in the HSI-SR problem, which has improved in all three simulated datasets. In particular, the PSNR on the Pavia University dataset has increased by 4.46dB. Besides, we observe that TNN has more advantages than MNN from Table VI. For example, SAM in the Pavia dataset increased by nearly 1, and other values have improved to a certain extent.

TABLE V
ANALYSIS OF THE REGULARIZATION POINT-1

Dataset		PSNR	RMSE	SSIM	ERGAS	SAM
Pavia University	$\lambda=0$	37.11	5.24	0.94	0.75	5.13
	$\lambda \neq 0$	**41.57**	**2.9**	**0.98**	**0.40**	**3.02**
Indian Pines	$\lambda=0$	29.01	11.14	0.79	2.94	4.8
	$\lambda \neq 0$	**30.18**	**9.67**	**0.83**	**2.52**	**4.20**
Harvard-imgg9	$\lambda=0$	50.91	0.87	0.98	1.28	3.56
	$\lambda \neq 0$	**51.52**	**0.82**	**0.99**	**1.19**	**3.33**

E. Convergence Behavior and Running Time Comparison

1) Convergence Behavior: In this part, we empirically analyze the convergence of the propsoed Algorithm 2. Fig. 12 (a), Fig. 12 (b), and Fig. 12 (c) show the $RelCha$ on Pavia University, Indian Pines, and Harvard dataset, respectively. Each $RelCha$ rapidly approaches to zero, confirming the global convergence of Algorithm 2.
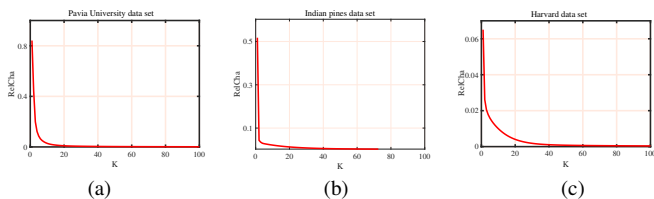

Fig. 12. $RelCha$ in each iteration of Algorithm 2 on three datasets. Convergence curve of (a) Pavia University dataset, (b) Harvard dataset, and (c) CAVE dataset.

2) Runing Time Comparison: In this part, we compare the runtime results of all test methods, as shown in Table VII, where the time of each dataset is the average of the time that the dataset runs under four noise levels. We highlight the least and second running times in bold and underlined, respectively. From the table, we find that CNMF has the least running time,

TABLE VI
ANALYSIS OF THE REGULARIZATION POINT-2

Dataset		PSNR	RMSE	SSIM	ERGAS	SAM
Pavia University	MNN	38.94	3.86	0.96	0.54	4
	TNN	**41.57**	**2.9**	**0.98**	**0.40**	**3.02**
Indian Pines	MNN	29.73	10.01	0.82	2.62	4.31
	TNN	**30.18**	**9.67**	**0.83**	**2.52**	**4.20**
Harvard-imgg9	MNN	51.35	0.81	0.98	1.2	3.4
	TNN	**51.52**	**0.82**	**0.99**	**1.19**	**3.33**

while S^4-LRR has the most running time. Besides, NLSTF, HySure, and CSTF run in an acceptable time range. The running time of the proposed IR-TenSR is less than LTTR and S^4-LRR and fine.

TABLE VII
COMPARISONS OF RUNNING TIME FOR ALL TEST METHODS (IN SECONDS)

Method	Time (s)			
	Pavia University	CAVE	Indian Pines	Realdata
CNMF [48]	**5.35**	**21.84**	2.29	**7.70**
HySure [53]	7.62	42.40	**0.95**	41.18
CSTF [37]	10.67	<u>31.59</u>	9.33	132.18
NLSTF [35]	<u>6.54</u>	205.68	<u>1.83</u>	<u>16.90</u>
LTTR [44]	192.07	172.62	9.22	66.83
LTMR [61]	65.08	123.67	28.40	41.10
S^4-LRR [30]	674.70	6633.00	705.36	384.50
IR-TenSR	124.89	152.86	123.02	74.20

VI. CONCLUSION

In this work, we develop the IR-TenSR for HSI-SR. The suggested TenSR-based regularization model concatenates the global spectral-spatial correlation and nonlocal self-similarity property of HR-HSI. Specifically, to fully describe the correlation in spectrum and space, we use the TenSR to represent the HR-HSI. Under the framework of TenSR, we introduce the nonlocal low-rank regularization to constrain the tensor coefficient image. Equipped with that, we design an iterative regularization procedure to exploit the residual information of acquired MSI and HSI. Finally, we obtain the iterative regularization algorithm by embedding the algorithm for the TenSR-based regularization model into the iterative regularization procedure. Extensive comparative experimental tests on one real dataset and three simulated datasets demonstrate the advantages of the proposed IR-TenSR compared with the existing state-of-the-art HSI-SR methods, both visual and

quantitative results. Finally, some discussions further verify the rationality and effectiveness of the proposed IR-TenSR.

REFERENCES

[1] N. Yokoya, C. Grohnfeldt, and J. Chanussot, "Hyperspectral and multi-spectral data fusion: a comparative review of the recent literature," *IEEE Geosci. Remote Sens. Magaz.*, vol. 5, no. 2, pp. 29–56, 2017.

[2] G. Baier, A. Deschemps, M. Schmitt, and N. Yokoya, "Synthesizing optical and sar imagery from land cover maps and auxiliary raster data," *IEEE Trans. Geosci. Remote Sens.*, vol. 60, pp. 1–12, 2022.

[3] W. He, N. Yokoya, and X. Yuan, "Fast hyperspectral image recovery of dual-camera compressive hyperspectral imaging via non-iterative subspace-based fusion," *IEEE Trans. Image Process.*, vol. 30, pp. 7170–7183, 2021.

[4] W. He, N. Yokoya, L. Yuan, and Q. Zhao, "Remote sensing image reconstruction using tensor ring completion and total variation," *IEEE Trans. Geosci. Remote Sens.*, vol. 57, no. 11, pp. 8998–9009, 2019.

[5] D. Hong, L. Gao, J. Yao, B. Zhang, A. Plaza, and C. Jocelyn, "Graph convolutional networks for hyperspectral image classification," *IEEE Trans. Geosci. Remote Sens.*, vol. 59, no. 7, pp. 5966–5978, 2021.

[6] X.-Y. Cao, J. Yao, Z.-B. Xu, and D.-Y. Meng, "Hyperspectral image classification with convolutional neural network and active learning," *IEEE Trans. Geosci. Remote Sens.*, vol. 58, no. 7, pp. 4604–4616, 2020.

[7] L. Zhang, W. Wei, C. Bai, Y. Gao, and Y. Zhang, "Exploiting clustering manifold structure for hyperspectral imagery super-resolution," *IEEE Trans. Image Process.*, vol. 27, no. 12, pp. 5969–5982, 2018.

[8] J.-L. Xiao, T.-Z. Huang, L.-J. Deng, Z.-C. Wu, and G. Vivone, "A new context-aware details injection fidelity with adaptive coefficients estimation for variational pansharpening," *IEEE Trans. Geosci. Remote Sens.*, 2022, doi: 10.1109/TGRS.2022.3154480.

[9] T.-J. Zhang, L.-J. Deng, T.-Z. Huang, J. Chanussot, and G. Vivone, "A triple-double convolutional neural network for panchromatic sharpening," *IEEE Trans. Neural Netw. Learn. Syst.*, 2022, doi: 10.1109/TNNLS.2022.3155655.

[10] N. Yokoya, K. Yamanoi, W. He, G. Baier, B. Adriano, H. Miura, and S. Oishi, "Breaking limits of remote sensing by deep learning from simulated data for flood and debris-flow mapping," *IEEE Trans. Geosci. Remote Sens.*, vol. 60, pp. 1–15, 2022.

[11] R.-W. Dian, S.-T. Li, and X. Kang, "Regularizing hyperspectral and multispectral image fusion by cnn denoiser," *IEEE Trans. Neural Netw. Learn. Syst.*, vol. 32, no. 3, pp. 1124–1135, 2020.

[12] R.-W. Dian, S.-T. Li, A.-J. Guo, and L.-Y. Fang, "Deep hyperspectral image sharpening," *IEEE Trans. Neural Netw. Learn. Syst.*, vol. 29, no. 11, pp. 5345–5355, 2018.

[13] H.-P. Guo, P.-X. Zhuang, and Y.-C. Guo, "Bayesian pan-sharpening with multi-order gradient-based deep network constraints," *IEEE J. Sel. Top. Appl. Earth Obs. and Remote Sens.*, vol. 13, pp. 950–962, 2020.

[14] X.-Y. Fu, W. Wang, Y. Huang, X.-H. Ding, and J. Paisley, "Deep multi-scale detail networks for multi-band spectral image sharpening," *IEEE Trans. Neural Netw. Learn. Syst.*, vol. 32, no. 5, pp. 2090–2104, 2021.

[15] Y. Yang, H.-Y. Lu, S.-Y. Huang, and W. Tu, "Remote sensing image fusion based on fuzzy logic and salience measure," *IEEE Geosci. Remote Sens. Lett.*, vol. 17, no. 11, pp. 1943–1947, 2020.

[16] L.-J. Deng, G. Vivone, C. Jin, and J. Chanussot, "Detail injection-based deep convolutional neural networks for pansharpening," *IEEE Trans. Geosci. Remote Sens.*, vol. 59, no. 8, pp. 6995–7010, 2021.

[17] J.-F. Hu, T.-Z. Huang, L.-J. Deng, T.-X. Jiang, G. Vivone, and J. Chanussot, "Hyperspectral image super-resolution via deep spatiospectral attention convolutional neural networks," *IEEE Trans. Neural Netw. Learn. Syst.*, 2021, doi:10.1109/TNNLS.2021.3084682.

[18] Z.-R. Jin, L.-J. Deng, T.-J. Zhang, and X. Jin, "Bam: Bilateral activation mechanism for image fusion," *in proc. ACM Int. Conf. Multimedia (ACM MM)*, 2021, doi: 10.1145/3474085.3475571.

[19] Y.-D. Wang, L.-J. Deng, T.-J. Zhang, and X. Wu, "Ssconv: Explicit spectral-to-spatial convolution for pansharpening," *in proc. ACM Int. Conf. Multimedia (ACM MM)*, p. DOI: 10.1145/3474085.3475600., 2021.

[20] X. Wu, T.-Z. Huang, L.-J. Deng, and T.-J. Zhang, "Dynamic cross feature fusion for remote sensing pansharpening," 2021, pp. 14 687–14 696.

[21] C. Jin, L.-J. Deng, T.-Z. Huang, and G. Vivone, "Laplacian pyramid networks: A new approach for multispectral pansharpening," *Inf. Fusion*, vol. 78, pp. 158–170, 2022.

[22] X.-Y. Cao, X.-Y. Fu, D.-F. Hong, Z.-B. Xu, and D.-Y. Meng, "Pancsc-net: A model-driven deep unfolding method for pansharpening," *IEEE Trans. Geosci. Remote Sens.*, pp. 1–13, 2021.

[23] X.-Y. Fu, Z.-H. Lin, Y. Huang, and X.-H. Ding, "A variational pan-sharpening with local gradient constraints," *in Proc. IEEE Conf. Comput. Vis. Pattern Recognit. (CVPR)*, pp. 10 257–10 266, 2019, doi: 10.1109/CVPR.2019.01051.

[24] J.-F. Yang, X.-Y. Fu, Y.-W. Hu, Y. Huang, X.-H. Ding, and J. Paisley, "Pannet: A deep network architecture for pan-sharpening," *in proc. IEEE Int. Conf. Comput. Vis. (ICCV)*, pp. 1753–1761, 2017, doi: 10.1109/ICCV.2017.193.

[25] Y. Yang, C.-X. Wan, S.-Y. Huang, H.-Y. Lu, and W.-G. Wan, "Pansharpening based on low-rank fuzzy fusion and detail supplement," *IEEE J. Sel. Top. Appl. Earth Obs. and Remote Sens.*, vol. 13, pp. 5466–5479, 2020.

[26] L.-R. Gao, D.-F. Hong, J. Yao, B. Zhang, P. Gamba, and J. Chanussot, "Spectral superresolution of multispectral imagery with joint sparse and low-rank learning," *IEEE Trans. Geosci. Remote Sens.*, vol. 59, no. 3, pp. 2269–2280, 2021.

[27] Y. Qu, H.-R. Qi, and C. Kwan, "Unsupervised sparse dirichlet-net for hyperspectral image super-resolution," 2018, pp. 2511–2520.

[28] L. Zhang, J. Nie, W. Wei, Y. Zhang, S. Liao, and L. Shao, "Unsupervised adaptation learning for hyperspectral imagery super-resolution," pp. 3070–3079, 2020.

[29] E. Lanaras, C. Baltsavias, and K. Schindler, "Hyperspectral super-resolution by coupled spectral unmixing," *in proc. IEEE Int. Conf. Comput. Vis. (ICCV)*, pp. 3586–3594, 2015.

[30] J. Xue, Y.-Q. Zhao, Y. Bu, W. Liao, J. C.-W. Chan, and W. Philips, "Spatial-spectral structured sparse low-rank representation for hyper-spectral image super-resolution," *IEEE Trans. Image Process.*, vol. 30, pp. 3084–3097, 2021.

[31] Y. Xu, Z. Wu, J. Chanussot, and Z. Wei, "Nonlocal patch tensor sparse representation for hyperspectral image super-resolution," *IEEE Trans. Image Process.*, vol. 28, no. 6, pp. 3034–3047, 2019.

[32] X. Li, Y. Yuan, and Q. Wang, "Hyperspectral and multispectral image fusion via nonlocal low-rank tensor approximation and sparse represen-tation," *IEEE Trans. Geosci. Remote Sens.*, vol. 59, no. 1, pp. 550–562, 2021.

[33] J. Liu, Z. Wu, L. Xiao, J. Sun, and H. Yan, "A truncated matrix decomposition for hyperspectral image super-resolution," *IEEE Trans. Image Process.*, vol. 29, pp. 8028–8042, 2020.

[34] W. Wan, W. Guo, J. Liu, and H. Huang, "Non-local blind hyperspectral image super-resolution via 4d sparse tensor factorization and low-rank," *Inverse Prob. Imaging*, vol. 14, no. 2, pp. 339–361, 2020.

[35] R. Dian, S. Li, L. Fang, T. Lu, and J. M. Bioucas-Dias, "Nonlocal sparse tensor factorization for semiblind hyperspectral and multispectral image fusion," *IEEE Trans. Cyber.*, vol. 50, no. 10, pp. 4469–4480, 2020.

[36] R.-W. Dian, L.-Y. Fang, and S.-T. Li, "Hyperspectral image super-resolution via non-local sparse tensor factorization," *in Proc. IEEE Conf. Comput. Vis. Pattern Recog. (CVPR)*, pp. 5344–5353, 2017.

[37] S.-T. Li, R.-W. Dian, L.-Y. Fang, and J. M. Bioucas-Dias, "Fusing hyperspectral and multispectral images via coupled sparse tensor fac-torization," *IEEE Trans. Image Process.*, vol. 27, no. 8, pp. 4118–4130, 2018.

[38] T. Xu, T.-Z. Huang, L.-J. Deng, X.-L. Zhao, and J. Huang, "Hyper-spectral image superresolution using unidirectional total variation with tucker decomposition," *IEEE J. Sel. Top. Appl. Earth Obs. and Remote Sens.*, vol. 13, pp. 4381–4398, 2020.

[39] J. Xue, Y. Zhao, W. Liao, J. C.-W. Chan, and S. G. Kong, "Enhanced sparsity prior model for low-rank tensor completion," *IEEE Trans. Neural Netw. Learn. Syst.*, vol. 31, no. 11, pp. 4567–4581, 2020.

[40] C. I. Kanatsoulis, X. Fu, N. D. Sidiropoulos, and W.-K. Ma, "Hyperspec-tral super-resolution: A coupled tensor factorization approach," *IEEE Trans. Signal Process.*, vol. 66, no. 24, pp. 6503–6517, 2018.

[41] Y. Xu, Z. Wu, J. Chanussot, P. Comon, and Z. Wei, "Nonlocal coupled tensor cp decomposition for hyperspectral and multispectral image fusion," *IEEE Trans. Geosci. Remote Sens.*, vol. 58, no. 1, pp. 348–362, 2020.

[42] J. Xue, Y. Zhao, S. Huang, W. Liao, J. C.-W. Chan, and S. G. Kong, "Multilayer sparsity-based tensor decomposition for low-rank tensor completion," *IEEE Trans. Neural Netw. Learn. Syst.*, pp. 1–15, 2021.

[43] M. Ding, X. Fu, T.-Z. Huang, J. Wang, and X.-L. Zhao, "Hyperspectral super-resolution via interpretable block-term tensor modeling," *IEEE J. Sel. Topics Signal Process.*, vol. 15, no. 3, pp. 641–656, 2021.

[44] R.-W. Dian, S.-T. Li, and L.-Y. Fang, "Learning a low tensor-train rank representation for hyperspectral image super-resolution," *IEEE Trans. Neur. Net. Lear. Syst*, vol. 30, no. 9, pp. 2672–2683, 2019.

[45] Y. Xu, Z.-B. Wu, J. Chanussot, and Z.-H. Wei, "Hyperspectral images super-resolution via learning high-order coupled tensor ring represen-

tation," *IEEE Trans. Neural Netw. Learn. Syst.*, vol. 31, no. 11, pp. 4747–4760, 2020.

[46] W. He, Y. Chen, N. Yokoya, C. Li, and Q. Zhao, "Hyperspectral super-resolution via coupled tensor ring factorization," *Pattern Recog.*, vol. 122, p. 108280, 2022.

[47] Y. Chen, J.-S. Zeng, W. He, X.-L. Zhao, and T.-Z. Huang, "Hyperspectral and multispectral image fusion using factor smoothed tensor ring decomposition," *IEEE Trans. Geosci. Remote Sens.*, pp. 1–17, 2021, doi: 10.1109/TGRS.2021.3114197.

[48] N. Yokoya, T. Yairi, and A. Iwasaki, "Coupled nonnegative matrix factorization unmixing for hyperspectral and multispectral data fusion," *IEEE Trans. Geosci. Remote Sens.*, vol. 50, no. 2, pp. 528–537, 2012.

[49] C.-H. Lin, F. Ma, C.-Y. Chi, and C.-H. Hsieh, "A convex optimization-based coupled nonnegative matrix factorization algorithm for hyperspectral and multispectral data fusion," *IEEE Trans. Geosci. Remote Sens.*, vol. 56, no. 3, pp. 1652–1667, 2018.

[50] Q. Wei, J. Bioucas-Dias, N. Dobigeon, J. Y. Tourneret, M. Chen, and S. Godsill, "Multiband image fusion based on spectral unmixing," *IEEE Trans. Geosci. Remote Sens.*, vol. 54, no. 12, pp. 7236–7249, 2016.

[51] Y. Zhou, L.-Y. Feng, C.-P. Hou, and S.-Y. Kung, "Hyperspectral and multispectral image fusion based on local low rank and coupled spectral unmixing," *IEEE Trans. Geosci. Remote Sens.*, vol. 55, no. 10, pp. 5997–6009, 2017.

[52] M. A. Veganzones, M. Simões, G. Licciardi, N. Yokoya, J. M. Bioucas-Dias, and J. Chanussot, "Hyperspectral super-resolution of locally low rank images from complementary multisource data," *IEEE Trans. Image Process.*, vol. 25, no. 1, pp. 274–288, 2016.

[53] M. Simões, J. Bioucas-Dias, L. B. Almeida, and J. Chanussot, "A convex formulation for hyperspectral image superresolution via subspace-based regularization," *IEEE Trans. Geosci. Remote Sens.*, vol. 53, no. 6, pp. 3373–3388, 2015.

[54] Q. Wei, J. Bioucas-Dias, N. Dobigeon, and J. Y. Tourneret, "Hyperspectral and multispectral image fusion based on a sparse representation," *IEEE Trans. Geosci. Remote Sens.*, vol. 53, no. 7, pp. 3658–3668, 2015.

[55] W.-S. Dong, F.-Z. Fu, G.-M. Shi, X. Cao, J.-J. Wu, G.-Y. Li, and X. Li, "Hyperspectral image super-resolution via non-negative structured sparse representation," *IEEE Transactions on Image Processing*, vol. 25, no. 5, pp. 2337–2352, 2016.

[56] N. Akhtar, F. Shafait, and A. Mian, "Sparse spatio-spectral representation for hyperspectral image super-resolution," *in Proc. Eur. Conf. Comput. Vis. (ECCV)*, pp. 63–78, 2014.

[57] H. Xu, M. Qin, S. Chen, Y. Zheng, and J. Zheng, "Hyperspectral-multispectral image fusion via tensor ring and subspace decompositions," *IEEE J. Sel. Top. Appl. Earth Obs. and Remote Sens.*, vol. 14, pp. 8823–8837, 2021.

[58] J. Xue, Y. Zhao, W. Liao, and J. C.-W. Chan, "Nonlocal low-rank regularized tensor decomposition for hyperspectral image denoising," *IEEE Trans. Geosci. Remote Sens.*, vol. 57, no. 7, pp. 5174–5189, 2019.

[59] J. Lin, T.-Z. Huang, X.-L. Zhao, T.-X. Jiang, and L. Zhuang, "A tensor subspace representation-based method for hyperspectral image denoising," *IEEE Transactions on Geoscience and Remote Sensing*, vol. 59, no. 9, pp. 7739–7757, 2021.

[60] C. He, L. Sun, W. Huang, J. Zhang, Y. Zheng, and B. Jeon, "Tslrln: Tensor subspace low-rank learning with non-local prior for hyperspectral image mixed denoising," *Signal Process.*, vol. 184, p. 108060, 2021.

[61] R.-W. Dian and S.-T. Li, "Hyperspectral image super-resolution via subspace-based low tensor multi-rank regularization," *IEEE Trans. Image Process.*, vol. 28, no. 10, pp. 5135–5146, 2019.

[62] M. E. Kilmer and C. D. Martin, "Factorization strategies for third-order tensors," *Linear Algebra Appl.*, vol. 435, no. 3, pp. 641–658, 2011.

[63] C.-Y. Lu, J.-S. Feng, Y.-D. Chen, W. Liu, Z.-C. Lin, and S.-C. Yan, "Tensor robust principal component analysis with a new tensor nuclear norm," *IEEE Trans. Pattern Anal. Mach. Intell.*, vol. 42, no. 4, pp. 925–938, 2020.

[64] Y.-B. Zheng, T.-Z. Huang, X.-L. Zhao, T.-X. Jiang, T.-H. Ma, and T.-Y. Ji, "Mixed noise removal in hyperspectral image via low-fiberedrank regularization," *IEEE Trans. Geosci. Remote Sens.*, vol. 58, no. 1, p. 734–749, 2020.

[65] A. Chakrabarti and T. Zickler, "Statistics of real-world hyperspectral images," *in Proc. IEEE Conf. Comput. Vis. Pattern Recog. (CVPR)*, pp. 193–200, 2011.

[66] Y. Chen, T.-Z. Huang, W. He, N. Yokoya, and X.-L. Zhao, "Hyperspectral image compressive sensing reconstruction using subspace-based nonlocal tensor ring decomposition," *IEEE Trans. Geosci. Remote Sens.*, vol. 29, pp. 6813–6828, 2020.

[67] L.-J. Deng, G. Vivone, W. Guo, M. Dalla Mura, and J. Chanussot, "A variational pansharpening approach based on reproducible kernel hilbert space and heaviside function," *IEEE Trans. Image Process.*, vol. 27, no. 9, pp. 4330–4344, 2018.

[68] L.-J. Deng, W. Guo, and T.-Z. Huang, "Single image super-resolution via an iterative reproducing kernel hilbert space method," *IEEE Trans. Circ. Syst. Video Technol.*, vol. 26, no. 11, pp. 2001–2014, 2016.

[69] S. Osher, M. Burger, D. Goldfarb, J. Xu, and W. Yin, "An iterative regularization method for total variation-based image restoration," *Multiscale Model. Simul.*, vol. 4, no. 2, pp. 460–489, 2005.

[70] J. Nocedal and S. Wright, "Numerical optimization," *Springer*, 2006.

[71] Q. Wei, N. Dobigeon, and J. Y. Tourneret, "Fast fusion of multiband images based on solving a sylvester equation," *IEEE Trans. Image Process.*, vol. 23, pp. 1632–1636, 2015.

[72] F. Dell' Acqua, P. Gamba, A. Ferrari, J. A. Palmason, J. A. Benediktsson, and K. Arnason, "Exploiting spectral and spatial information in hyperspectral urban data with high resolution," *IEEE Geosci. Remote Sens. Lett.*, vol. 1, no. 4, pp. 322–326, 2004.

[73] R. O. Green, M. L. Eastwood, C. M. Sarture, T. G. Chrien, M. Aronsson, B. J. Chippendale, J. A. Faust, B. E. Pavri, C. J. Chovit, M. Solis, M. R. Olah, and O. Williams, "Imaging spectroscopy and the airborne visible/infrared imaging spectrometer (aviris)," *Remote Sens. Environment*, vol. 65, no. 3, pp. 227 – 248, 1998.

[74] Z. Wang, A. C. Bovik, H. R. Sheikh, and E. P. Simoncelli, "Image quality assessment: From error visibility to structural similarity," *IEEE Trans. Image Process.*, vol. 13, no. 4, p. 600–612, 2004.